Slip identification from HR-DIC/EBSD: Incorporating Crystal Plasticity constitutive laws

Dorian Depriester, Jean-Patrick Goulmy, Laurent Barrallier

International Journal of Solids and Structures 305 (2024) 113077

Contents lists available at ScienceDirect

International Journal of Solids and Structures

journal homepage: www.elsevier.com/locate/ijsolstr

Slip identification from HR-DIC/EBSD: Incorporating Crystal Plasticity constitutive laws

Dorian Depriester *, Jean-patrick Goulmy, Laurent Barrallier

Arts et Métiers Institute of Technology, MSMP, HESAM Université, F-13617 Aix-en-Provence, France

ARTICLE INFO

Dataset link: https://github.com/DorianDepriester/SSLIP-CP/

Keywords:
HR-DIC
EBSD
Slip systems
In situ tensile test
CPFEM
Strain hardening
Crystal Plasticity

ABSTRACT

It is well known that dislocation slip plays a major role in plastic deformation of polycrystals. Depending on the crystal's symmetry, only a limited number of Slip Systems (SSs) are possible, and their activities depend on the crystal orientation with respect to the applied stress. High Resolution Digital Image Correlation (HR-DIC) can be used to get the full-field measurements of displacement fields on the surface of the strained material during an in situ tensile test, whereas the EBSD technique provides local crystallographic orientations. Therefore, coupling them can lead to full description of the local slip activities. Recently, an algorithm (named SSLIP) was proposed in the literature to automatically estimate the plastic activity from HR-DIC and EBSD data. The aim of the present paper is first to improve this algorithm so that it works for incremental straining, and to propose a way to take account for the anisotropic behaviour through a well-known set of Crystal Plasticity (CP) constitutive laws. It is shown that slip identification, together with those CP laws, can be used to estimate the tensile stress at grain scale. The influence of the DIC resolution is investigated and "correction rules" for small grains are proposed. Finally, the experimental results are compared against those found using the CP Finite Element Method (CPFEM), showing good consistency, specially in terms of active SSs and local stress.

1. Introduction

Understanding the mechanical behaviour of bulk materials requires the investigation of phenomena occurring at microscopic scale. For ductile polycrystalline materials, such as metals, it is well known that the plastic deformation is mainly governed by dislocation slips at grain scale. Studying such phenomena is usually referred to as Crystal Plasticity (CP) analysis, whose most historical contribution is due to Erich Schmid in 1935. At room temperature, slip can only occur along certain directions and certain planes, depending on the crystal symmetry. Each pair of possible direction/plane is referred to as a slip system (SS). For Face Centred Cubic (FCC) materials, those SSs are given by the combinations of $\{111\}\langle\bar{1}10\rangle$ families, whereas those for Body Centred Cubic (BCC) are combinations of $\{110\}\langle\bar{1}11\rangle$, $\{211\}\langle\bar{1}11\rangle$ and $\{321\}\langle\bar{1}11\rangle$ families (Jackson, 2012, Chap. 7).

Analysing these SSs is of great importance for investigating the plastic-induced phenomena. For instance, Salvini et al. (2024) evidenced a relationship between damage initiation and plastic incompatibilities near Grain Boundaries (GBs). Experimental analyses of SSs require microstructural characterisation, usually made with Scanning Electron Microscopy (SEM) imaging. In order to facilitate the investigation of slip activities at different strain levels, authors usually perform in situ tensile tests within the chamber of SEMs. SEM images can then be used to perform Digital Image Correlation (DIC) at grain scale, thus allowing to measure the local strain in the apparent microstructure (Di Gioacchino and Quinta da Fonseca, 2015; Mello et al., 2017; Guan et al., 2017; Thomas et al., 2019; Sperry et al., 2020; Di Gioacchino et al., 2020; Thiruselvam et al., 2021; Guan et al., 2021; Goulmy et al., 2022; León-Cázares et al., 2023; Stinville et al., 2023, and references therein). Di Gioacchino and Quinta da Fonseca (2015) demonstrated that the localisation bands, evidenced by High Resolution DIC (HR-DIC), were parallel to the trace of the slip planes (intersection of slip planes with the imaged surface of the material). Therefore, by analysing the orientations of those localisation bands, one can estimate which plane family is active, but not the direction. León-Cázares et al. (2023) recently proposed to perform Fast Fourier Transforms (FFTs) on the DIC maps in order to automatically detect the localisation bands and characterise their orientations; it allowed to detect and process thousands of slip traces at once on FCC Ni-based superalloy. Alternatively, some authors used the Radon (Sperry et al., 2020) or the Hough (Charpagne et al., 2020) transforms to automatically detect the localisation bands from DIC maps. Chen and Daly (2017) have introduced the "Relative Displacement Ratio" (RDR) method, which compares the ratio of displacement components, evidenced by HR-DIC, with that of the Burger's vector of each SS to determine which

* Corresponding author.
E-mail addresses: dorian.depriester@ensam.eu (D. Depriester), jean-patrick.goulmy@ensam.eu (J.-p. Goulmy), laurent.barrallier@ensam.eu (L. Barrallier).

https://doi.org/10.1016/j.ijsolstr.2024.113077
Received 24 April 2024; Received in revised form 11 September 2024; Accepted 15 September 2024
Available online 21 September 2024

Notations

Mathematical conventions

In the present paper, the ISO 80000–2 font convention is used: lowercased boldface denotes a vector (e.g.: $\boldsymbol{s}$); uppercased boldface denotes a matrix (e.g.: $\boldsymbol{H}$); sans-serif boldface denotes a tensor (e.g.: $\boldsymbol{F}$) whereas light font denotes a scalar value (e.g.: a) or the components of a tensor/matrix/vector (e.g.: S_{ij}^{α}). The Einstein's summation convention is used.

Nomenclature

$\boldsymbol{F}$	Displacement gradient
$\Delta\boldsymbol{F}$	Increment of displacement gradient
$\dot{\gamma}^{\alpha}$	Shear rate on slip system α
$\Delta\gamma^{\alpha}$	Increment of shear (slip activity) in slip system α
$\boldsymbol{H}$	Latent hardening matrix
$\boldsymbol{L}$	Plastic velocity gradient
$\boldsymbol{M}$	Matrix of crystallographic orientation
N	Number of investigated slip systems
p	Number of active slip systems
s^{α}	CRSS of slip system α
$\boldsymbol{S}^{\alpha}$	Schmid tensor of slip system α
τ^{α}	Resolved shear stress on slip system α

SS may be active or not. Alternatively, Bourdin et al. (2018) have proposed the Heaviside DIC method, which automatically detects the discontinuities in the gradient field, thus allowing to detect the localisation bands, hence the slip traces. Nevertheless, these methods only work if the localisation bands are well defined. Therefore, Vermeij et al. (2023) have proposed a method, named SSLIP, to automatically identify the slip activity from in situ DIC coupled with Electron Backscattered Diffraction (EBSD) technique. Given a single crystallographic orientation (at each datapoint of the EBSD map), the SSLIP method consists in minimising the sum of absolute shears along each SS such that the corresponding gradient is close to that given by DIC. This allowed to successfully characterise the activity of each SS in FCC Ni-based superalloy and BCC ferrite. More recently, Vermeij et al. (2024) have proposed an updated version of SSLIP, named +SSLIP, which only considers SSs that are compatible with the orientations of the localisation bands, thus reducing the dimensions of the optimisation problem. These orientations were characterised with the aid of the Radon transform. Vermeij et al. showed that this approach was very promising for materials with large number of SSs, such as Hexagonal close-packed (HCP) materials. Nevertheless, the criterion used in SSLIP and +SSLIP (sum of absolute values of shear strain on each SS) is only valid if the strain hardening is neglected and if the Critical Resolved Shear Stress (CRSS) of all SSs are the same. Therefore, it is not suitable for more anisotropic materials, such as numerous HCP crystals. For instance, Wang et al. (2017) reported that the CRSSs in commercially pure titanium for basal ($\{0001\}\langle 1\bar{2}10\rangle$), prismatic ($\{10\bar{1}0\}\langle 1\bar{2}10\rangle$) and pyramidal ($\{10\bar{1}1\}\langle 2\bar{1}\bar{1}\bar{3}\rangle$) SSs were 127 MPa, 96 MPa and >240 MPa, respectively. Hence the well-known "soft" $\langle 1\bar{2}10\rangle$ and "hard" $\langle 2\bar{1}\bar{1}\bar{3}\rangle$ directions of α titanium. In addition, during plastic deformation, strain hardening occurs while grains undergo crystallographic reorientation; which in turn can change the plastic behaviour of crystals at subsequent straining increments. For instance, Zecevic et al. (2018) showed that, at the early stages of extrusion of HCP Mg-4%Li, basal slip was predominant, whereas prismatic became predominant at larger deformation.

Today's performances of computers have allowed the emergence and the generalisation of CP Finite Element Method (CPFEM). It can be used to simulate the plastic behaviour of polycrystals, taking into account the CP constitutive laws and provides extensive data about plastic activities at local scale. EBSD-based CPFEM is usually made under the near-plane-stress assumption (Héripré et al., 2007; Guery et al., 2016a; Kawano et al., 2019; Githens et al., 2020; Depriester et al., 2023), which allows to consider only one element in thickness (Héripré et al., 2007). Therefore, Depriester and Kubler (2020) recently proposed a software to generate conforming meshes from grains reconstructed with MTEX (Bachmann et al., 2011) in an automatic and flexible way, resulting in a one-element-thick mesh with smooth and accurate descriptions of GBs. Under the aforementioned near-plane-stress assumption, the effect of microstructure underneath the EBSD-mapped surface is neglected. Githens et al. (2020) showed that this assumption was reasonable in terms of strain calculations, but that it can impair the apparent slip activities. However, the estimation of CP parameters is usually challenging. In an earlier work, the present authors (Depriester et al., 2023) calibrated a CP constitutive law on pure copper by performing an inverse analysis based on CPFEM. They showed that the most active SSs in CPFEM were consistent with the slip traces evidenced by HR-DIC, although some discrepancy was reported in terms of local strain. A coupled HR-DIC/CPFEM approach was also used by Guery et al. (2016b) to study the slip activity in a 316LN austenitic stainless steel; at local scale (i.e. for each Gauss point in CPFEM), they showed that, on average, only four SSs were active at once during the in situ tensile test according to CPFEM. They also showed that some SSs were reported as active according to CPFEM, whereas no evidence of such activity was made experimentally (no slip trace).

On the basis of the preceding considerations, to the best authors' knowledge, there is no tool available in the literature able to fully unravel active SSs from coupled EBSD/HR-DIC data, which supports the following requirements:

- incremental straining;
- strain hardening and crystallographic reorientations due to plastic strain;
- slip anisotropies (different CRSS values).

Therefore, the aim of this work is first to propose and to assess such an algorithm. In addition, since HR-DIC can be performed at different resolutions, their influence on the results from this algorithm should be investigated. As a result, this paper is divided as follows: the material used as an application in this work is presented in Section 2 whereas the fundamentals of CP are recalled in Section 3. Then, two different approaches (namely the L_1 and the Energy methods), derived from the SSLIP method, are detailed in Section 4. The results of the two different approaches are discussed and compared in Section 5 whereas the fundamental difference between them is detailed in Section 6.1. The influence of the image resolution on the quality of the results from the proposed approaches is investigated in Section 6.2. The present results are then compared against CPFEM simulations. Finally, the computational performances of the proposed methods are discussed in Section 6.4.

2. Materials and methods

2.1. Materials

In a previous work, Goulmy et al. (2022) performed an in situ tensile test on commercially pure copper in the chamber of a SEM. Thanks to the rough surface of the sample (because of slight chemical etching), HR-DIC was performed from stitched SEM micrographs. In the present paper, EBSD data of the initial microstructure and HR-DIC measurements were taken from this prior work. The macroscopic tensile curve (measured by the in situ tensile apparatus) and the EBSD map of the Region of Interest (RoI) are provided in Fig. 1. The tensile direction (denoted $\boldsymbol{e}_1$ below) is represented as horizontal in Fig. 1(b).

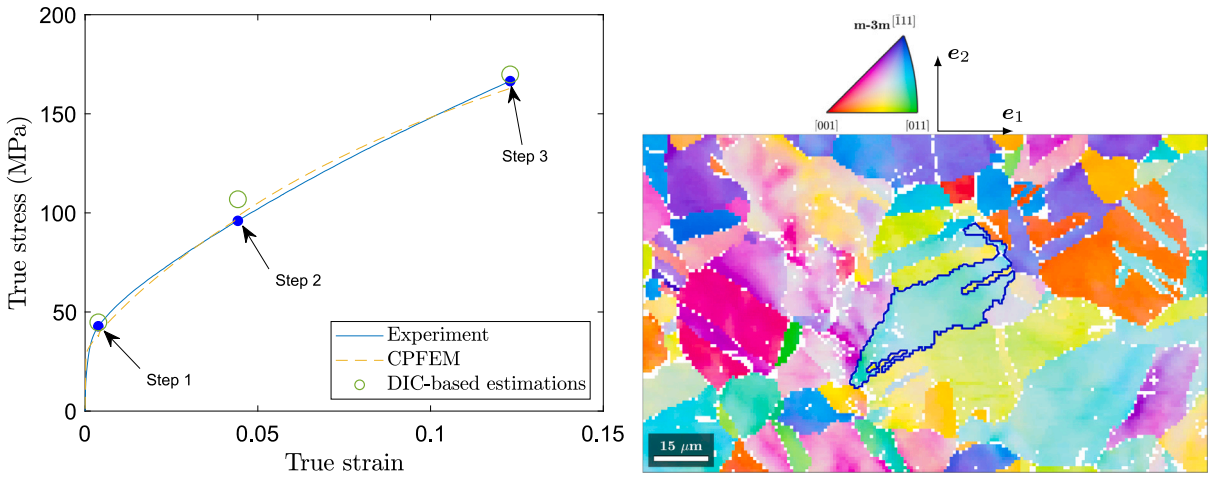

(a) Tensile curve (b) EBSD map

Fig. 1. Experimental data from in situ tensile test of pure copper. The colours in the EBSD map (b) relates to the crystallographic orientation with respect to the loading direction (e_1). The grain highlighted in blue is used in Sections 5.1 and 6.3.

Table 1
CP parameters calibrated on commercially pure copper by Depriester et al. (2023).

q	h_0	s_0	s_∞	a
1.702	309.5 MPa	12.22 MPa	121.8 MPa	2.192

Table 2
DIC parameters used in this work.
Source: Taken from Goulmy et al. (2022).

Work. dist.	Dwell time	Acc. voltage	Img. Resol.	Img. integration
12.1 mm	2.89 μs	10 kV	19 nm px^{-1}	8

All the CP-related parameters (see Section 3 for details) of the aforementioned material were calibrated in a prior work (Depriester et al., 2023), as recalled in Table 1.

2.2. DIC measurements

Let $\boldsymbol{X}$ be the coordinate vector of a given point in reference state (unstrained), and $\boldsymbol{x}$ the vector position in deformed state. The gradient tensor is defined as:

$$\boldsymbol{F} = \frac{\partial \boldsymbol{x}}{\partial \boldsymbol{X}} \tag{1}$$

Because DIC is performed in 2D on the visible (outer) surface only, only F_{11}, F_{12}, F_{21} and F_{22} can be computed from DIC.

In Goulmy et al. (2022), HR-DIC was performed at three straining levels (called steps), as recalled in Fig. 1(a) (see solid blue dots). For each step, high resolution imaging was achieved by stitching 48 SEM images, obtained using the secondary electrons detector of a Field Emission Gun (FEG) of a JEOL JSM-7001F in high vacuum (HV) mode. This resulted in images of size 177×100 μm, containing 112 individual grains. The speckle used for DIC was obtained with a slight chemical etching of the imaged surface of the sample. SEM operating parameters are provided in Table 2. Based on the stitched images, local DIC was then performed with the Ncorr software (Blaber et al., 2015).

DIC comes with many parameters (displacement subset size, strain subset size, etc.), but all of them can somehow be gathered in the window size (Goulmy et al., 2022), denoted φ below. This parameter represents the extent of a pixel value's region of effect over the measured strain at nearby places. It was shown in the latter work that $\varphi = 1.3$ μm was the best compromise between resolution and stability, for it allowed to evidence localisation bands with reduced noises on the strain values. Therefore, in this paper, we use DIC measurements made with $\varphi = 1.3$ μm (except if mentioned); the corresponding values for $\boldsymbol{F}$ at each step are illustrated in Fig. 2. It is worth noticing the vertical artefacts on F_{11} and the horizontal ones on F_{12}, specially at early stages of the deformation (see Fig. 2(a)). These artefacts have been documented by Goulmy et al. (2022); the latter authors concluded that they were due to a slight drift of the beam during SEM imaging (rastering effect). They can easily be avoided in single images (Goulmy et al., 2024) but avoiding them in stitched images require more complex techniques (Maraghechi et al., 2019; Rouwane et al., 2024). However, because these artefacts seem to vanish at larger deformation (see Figs. 2(b) and 2(c)) they were neglected in the present work, although a mask was used to remove them from certain analyses (this will be mentioned in this case).

3. Theory

3.1. The Schmid theory

This section briefly recalls the Schmid theory for CP, which the proposed paper is based on.

Let $\boldsymbol{\tau}$ be the second-order Cauchy stress tensor. The resolved shear stress on SS α is:

$$\tau^\alpha = \boldsymbol{S}^\alpha : \boldsymbol{\tau} \tag{2}$$

where $\boldsymbol{S}^\alpha$ is the Schmid tensor for SS α, such that:

$$S^\alpha_{ij} = b^\alpha_i n^\alpha_j$$

where $\boldsymbol{b}^\alpha$ and $\boldsymbol{n}^\alpha$ are the slip direction and slip plane normal for SS α, respectively. In (2), " : " denotes the inner product of tensors:

$$\tau^\alpha = S^\alpha_{ij} \tau_{ij}$$

Let s^α be the CRSS of SS α. The latter is inactive if, and only if:

$$|\tau^\alpha| \leq s^\alpha$$

otherwise, slip occurs and the SS undergoes hardening (s^α increases); in this case, we have:

$$\tau^\alpha = \text{sign}\,(\dot{\gamma}^\alpha)\, s^\alpha \tag{3}$$

where $\dot{\gamma}^\alpha$ denotes the shear rate on SS α.

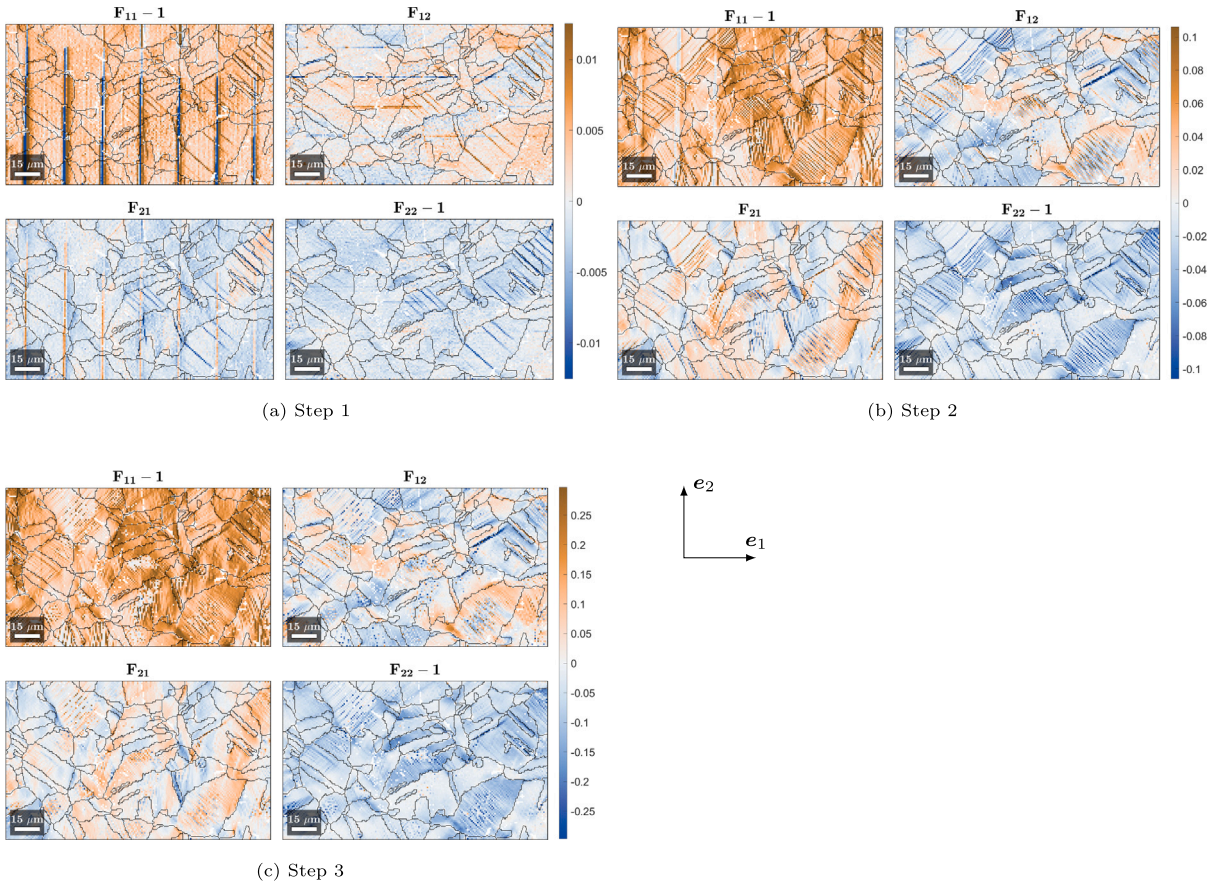

(a) Step 1

(b) Step 2

(c) Step 3

Fig. 2. Components of the gradient ($\boldsymbol{F}$) given by HR-DIC with $\varphi = 1.3\,\mu m$ at each step (blue dots in Fig. 1(a)). Grain boundaries are drawn in black.

3.2. Work hardening

This section presents the fundamental model of linear hardening, introducing the so-called latent hardening factor. The evolution law used in this paper for hardening moduli is also detailed.

A common hardening law, originally proposed by Peirce et al. (1982), gives the time derivative for CRSS of SS α as follows:

$$\dot{s}^\alpha = \sum_\beta H_{\alpha\beta} \left|\dot{\gamma}^\beta\right| \tag{4}$$

In (4), $H_{\alpha\alpha}$ denotes the self-hardening modulus of SS α, whereas $H_{\alpha\beta}$ denotes the latent-hardening modulus of SS β over SS α. Eq. (4) can be written in a matricial way:

$$\dot{\boldsymbol{s}} = \boldsymbol{H}\,|\dot{\boldsymbol{\gamma}}|$$

where $\boldsymbol{H}$ is the latent hardening matrix and $|\dot{\boldsymbol{\gamma}}|$ is a vector consisting in each absolute value of $\dot{\gamma}^\alpha$:

$$\dot{\boldsymbol{\gamma}} = \left[\left|\dot{\gamma}^1\right|, \quad \left|\dot{\gamma}^2\right|, \quad \ldots, \quad \left|\dot{\gamma}^N\right|\right]^\top$$

where N denotes the number of SSs (e.g. N=12 for FCC). The plastic velocity gradient is given by:

$$\boldsymbol{L} = \sum_\alpha \dot{\gamma}^\alpha \boldsymbol{S}^\alpha \tag{5}$$

In this paper, we assume that the hardening coefficients obey the following exponential rule, as proposed by Kalidindi et al. (1992):

$$H_{\alpha\beta} = \begin{cases} h_0 \left(1 - \frac{s^\beta}{s^\infty}\right)^a & \text{if } \boldsymbol{n}^\alpha = \boldsymbol{n}^\beta\,, \\ q h_0 \left(1 - \frac{s^\beta}{s^\infty}\right)^a & \text{otherwise.} \end{cases} \tag{6}$$

In (6), h_0, s^∞ and a are the initial hardening slope, the saturation stress and the exponent, respectively. q denotes the ratio of latent hardening rates to self hardening rates for non coplanar SSs (Kocks, 1970). As a reminder, the CP parameters for pure copper are provided in Table 1.

4. Calculation

4.1. Estimation of the plastic activity

In this section, two approaches are proposed to compute the slip activities from coupled EBSD/HR-DIC data.

Let $\dot{\boldsymbol{F}}$ be the material derivative of the gradient tensor, as defined in (1). We have (Nemat-Nasser, 2004, Chap. 5):

$$\dot{\boldsymbol{F}} \cdot \boldsymbol{F}^{-1} = \boldsymbol{L}$$

where "·" denotes the tensor product contracted once. Eq. (5) reads:

$$\dot{\boldsymbol{F}}\mathrm{d}t \cdot \boldsymbol{F}^{-1} = \sum_\alpha \dot{\gamma}^\alpha \mathrm{d}t \boldsymbol{S}^\alpha$$

where $\mathrm{d}t$ stands for the infinitesimal increment of time. Let $\boldsymbol{F}^\theta$ be the gradient tensor at time step θ. It comes:

$$\Delta\boldsymbol{F} \approx \sum_\alpha \Delta\gamma^\alpha \boldsymbol{S}^\alpha \cdot \boldsymbol{F}^\theta \tag{7}$$

where $\Delta\gamma^\alpha$ and $\Delta\boldsymbol{F}$ denote the increments of γ^α and $\boldsymbol{F}$ between two subsequent time step θ and $\theta+1$, respectively. Eq. (7) is equivalent to:

$$\Delta\boldsymbol{F} = \boldsymbol{\kappa}^\theta \cdot \Delta\boldsymbol{\gamma} \tag{8}$$

with

$$\Delta\boldsymbol{\gamma} = \left[\Delta\gamma^1, \quad \Delta\gamma^2, \quad \ldots, \quad \Delta\gamma^N\right]^\top$$

and $\boldsymbol{\kappa}^\theta \in \mathbb{R}^{2\times2\times N}$ being a 3rd-order tensor such that:

$$\kappa^\theta_{ij\alpha} = S^\alpha_{ik} F^\theta_{kj}$$

Alternatively, (8) can be vectorised as follows:

$$\boldsymbol{K}\,\Delta\boldsymbol{\gamma} = \begin{bmatrix} \Delta F_{11} \\ \Delta F_{21} \\ \Delta F_{12} \\ \Delta F_{22} \end{bmatrix} \tag{9}$$

where $\boldsymbol{K}$ is a $4 \times N$ matrix such that:

$$\boldsymbol{K} = \mathrm{Vec}\left(\boldsymbol{\kappa}^{\theta}\right) \tag{10}$$

$$= \begin{bmatrix} S_{11}^1 F_{11}^\theta + S_{12}^1 F_{21}^\theta & S_{11}^2 F_{11}^\theta + S_{12}^2 F_{21}^\theta & \dots & S_{11}^N F_{11}^\theta + S_{12}^N F_{21}^\theta \\ S_{21}^1 F_{12}^\theta + S_{12}^1 F_{21}^\theta & S_{21}^2 F_{12}^\theta + S_{12}^2 F_{21}^\theta & \dots & S_{21}^N F_{12}^\theta + S_{12}^N F_{21}^\theta \\ S_{11}^1 F_{11}^\theta + S_{22}^1 F_{22}^\theta & S_{11}^2 F_{11}^\theta + S_{22}^2 F_{22}^\theta & \dots & S_{11}^N F_{11}^\theta + S_{22}^N F_{22}^\theta \\ S_{21}^1 F_{12}^\theta + S_{22}^1 F_{22}^\theta & S_{21}^2 F_{12}^\theta + S_{22}^2 F_{22}^\theta & \dots & S_{21}^N F_{12}^\theta + S_{22}^N F_{22}^\theta \end{bmatrix} \tag{11}$$

As a reminder, out-of-plane components of $\boldsymbol{F}$ cannot be measured by DIC, hence the only four components in (9). It is worth mentioning that Goulmy et al. (2022) have proposed a method to estimate F_{33} under the generalised plane-strain assumption, but its value is coupled with other components (F_{11}, F_{12}, F_{21} and F_{22}); therefore, there is no advantage in taking this value into account.

In the present paper, "slip activity" refers to $\Delta\boldsymbol{\gamma}$, although it sometimes relates to its time derivative ($\dot{\boldsymbol{\gamma}}$) in the literature (Iftikhar et al., 2022, e.g.).

4.1.1. The L_1 method

The first approach investigated in this paper (named L_1 method hereafter) is similar to that originally proposed by Vermeij et al. (2023): one wants to minimise the total slip activity, keeping (9) true. This problem can be formatted as:

$$\Delta\boldsymbol{\gamma} = \underset{\boldsymbol{g}\in\mathbb{R}^N}{\mathrm{Arg\,min}} \left\{ \|\boldsymbol{g}\|_1 \text{ such that: } \boldsymbol{K}\boldsymbol{g} = \begin{bmatrix} \Delta F_{11} \\ \Delta F_{12} \\ \Delta F_{21} \\ \Delta F_{22} \end{bmatrix} \right\} \tag{12}$$

where $\|\boldsymbol{g}\|_1$ is the L_1-norm of $\boldsymbol{g}$ (sum of absolute values). Solving (12) is a non-linear minimisation with linear equality constraints. The main difference with the proposed approach, compared to that of Vermeij et al., is that the latter neglected $\boldsymbol{F}^\theta$ in (7). In addition, Vermeij et al. used intervals instead of strict equality in the constraints (11), taking into account measurement uncertainties on $\boldsymbol{F}$. This approach sounds fair, but wrong estimates of the uncertainties could lead to unrealistic results. Nonetheless, an extension of this approach is proposed in Appendix A.

4.1.2. The Energy method

This section proposes an alternative to the L_1 method, based on the plastic dissipated energy. Between time steps θ and $\theta+1$, if SS α is active, its slip work is:

$$w^\alpha = \int_{t^\theta}^{t^{\theta+1}} \tau^\alpha \dot{\gamma}^\alpha \mathrm{d}t \tag{13}$$

whilst (3) holds. Let s_θ^α be the CRSS of SS α at time step θ. We approximate $H_{\alpha\beta}$ as a constant between θ and $\theta+1$, and we assume that γ^β evolves monotonously between these time steps.[1] Therefore (4) reads:

$$s^\alpha(t) = \sum_\beta H_{\alpha\beta} \left|\gamma^\beta(t)\right| + s_\theta^\alpha \tag{14}$$

Eqs. (3), (13) and (14) give:

$$w^\alpha = \int_0^{\Delta\gamma^\alpha} \left(\sum_\beta H_{\alpha\beta} \left|\gamma^\beta\right| + s_0^\alpha \right) \mathrm{sign}\left(\mathrm{d}\gamma^\alpha\right) \mathrm{d}\gamma^\alpha \,. \tag{15}$$

[1] This requires the time step to be small enough to avoid back and forth shearing.

Because of the monotonous variation assumption above, we have:

$$\mathrm{sign}\left(\mathrm{d}\gamma^\alpha\right) \mathrm{d}\gamma^\alpha = \left|\mathrm{d}\gamma^\alpha\right| = \mathrm{d}\left|\gamma^\alpha\right|$$

Therefore, (15) becomes:

$$w^\alpha = \int_0^{|\Delta\gamma^\alpha|} \left(\sum_\beta H_{\alpha\beta} \left|\gamma^\beta\right| + s_0^\alpha \right) \mathrm{d}\left|\gamma^\alpha\right| \tag{16}$$

It is worth noticing that (16) is also valid if SS α is inactive ($\Delta\gamma^\alpha = 0 \implies w^\alpha = 0$). Hence, the dissipated plastic energy on all SSs is:

$$\begin{aligned} w &= \sum_\alpha \int_0^{|\Delta\gamma^\alpha|} \left(\sum_\beta H_{\alpha\beta} \left|\gamma^\beta\right| + s_0^\alpha \right) \mathrm{d}\left|\gamma^\alpha\right| \\ &= \int_0^{|\Delta\boldsymbol{\gamma}|} \left(\boldsymbol{H}\,|\boldsymbol{\gamma}| + s_0 \right) \mathrm{d}\,|\boldsymbol{\gamma}| \\ &= |\Delta\boldsymbol{\gamma}|^\top \left(\frac{\boldsymbol{H}}{2}\,|\Delta\boldsymbol{\gamma}| + s_0 \right) \end{aligned} \tag{17}$$

According to the minimum work principle, the increment of shear on each SS is so that w is minimal. Hence the second proposed method (named the Energy method hereafter) is based on minimising w, such that (11) holds, that is:

$$\Delta\boldsymbol{\gamma} = \underset{\boldsymbol{g}\in\mathbb{R}^N}{\mathrm{Arg\,min}} \left\{ |\boldsymbol{g}|^\top \left(\frac{\boldsymbol{H}}{2}\,|\boldsymbol{g}| + \boldsymbol{s} \right) \text{ such that: } \boldsymbol{K}\boldsymbol{g} = \begin{bmatrix} \Delta F_{11} \\ \Delta F_{12} \\ \Delta F_{21} \\ \Delta F_{22} \end{bmatrix} \right\} \tag{18}$$

Again, (18) is a non-linear minimisation problem with linear equality constraints.

4.2. Crystallographic reorientation

In this section, the crystallographic reorientation due to plastic strain is developed.

Given the plastic velocity gradient $\boldsymbol{L}$, the spin tensor is:

$$\boldsymbol{\omega} = \frac{1}{2}\left(\boldsymbol{L} - \boldsymbol{L}^\top\right) \tag{19}$$

Let $\boldsymbol{M}^{\theta+1}$ be the crystallographic orientation (represented as a rotation matrix) at increment $\theta+1$. It can be inferred from that at the previous increment ($\boldsymbol{M}^\theta$), taking into account the spin Hall (2013), Depriester et al. (2023):

$$\boldsymbol{M}^{\theta+1} = \boldsymbol{M}^\theta \cdot \exp\left(\boldsymbol{\omega}\mathrm{d}t\right) \tag{20}$$

where exp denotes the matrix exponential operator. Eqs. (5), (19) and (20) give:

$$\boldsymbol{M}^{\theta+1} = \boldsymbol{M}^\theta \cdot \exp\left(\sum_\alpha \left(\boldsymbol{S}^\alpha - \left(\boldsymbol{S}^\alpha\right)^\top \right) \Delta\gamma^\alpha \right) \tag{21}$$

4.3. Evolution of the CRSSs

In order to take into account the hardening evolution law (6), the harderning matrix should be updated at each step accordingly. Therefore, this section provides a method to estimate the evolution of CRSSs between two increments, based on the computed slip activities ($\Delta\gamma^\alpha$).

According to (14), we have[2]:

$$\boldsymbol{H}\left(\boldsymbol{s}\right) = \frac{\partial \boldsymbol{s}}{\partial\,|\boldsymbol{\gamma}|}\,.$$

Therefore, the Runge–Kutta 4 (RK4) algorithm (Press, 2007) can be used to estimate the CRSSs at time step $\theta+1$ as follows:

$$\boldsymbol{s}^{\theta+1} \approx \boldsymbol{s}^\theta + \bar{\boldsymbol{H}}\,|\Delta\boldsymbol{\gamma}| \tag{22}$$

[2] Recall that (14) is valid only if γ^α evolves monotonously.

with

$$\bar{\boldsymbol{H}} = \frac{1}{6}\left(\boldsymbol{H}_1 + 2\boldsymbol{H}_2 + 2\boldsymbol{H}_3 + \boldsymbol{H}_4\right) \tag{23}$$

and

$$\boldsymbol{H}_1 = \boldsymbol{H}\left(\boldsymbol{s}^\theta\right) \tag{24a}$$

$$\boldsymbol{H}_2 = \boldsymbol{H}\left(\boldsymbol{s}^\theta + \boldsymbol{H}_1 \left|\Delta\boldsymbol{\gamma}\right|/2\right) \tag{24b}$$

$$\boldsymbol{H}_3 = \boldsymbol{H}\left(\boldsymbol{s}^\theta + \boldsymbol{H}_2 \left|\Delta\boldsymbol{\gamma}\right|/2\right) \tag{24c}$$

$$\boldsymbol{H}_4 = \boldsymbol{H}\left(\boldsymbol{s}^\theta + \boldsymbol{H}_3 \left|\Delta\boldsymbol{\gamma}\right|\right) \tag{24d}$$

In Eqs. (24), $\boldsymbol{H}(\boldsymbol{s})$ denotes the hardening matrix computed depending on the CRSSs $\boldsymbol{s}$, with respect to the power-law Eq. (6).

4.4. Estimation of the stresses

Numerous approaches have been proposed in the literature to estimate the local stresses from DIC, but they are more suited when working with continuous relationship between strain rate and stress rate, for instance on elasticity (Roux et al., 2009) or anisotropic plasticity (Brosius et al., 2018). For more complex constitutive laws, such as CP, one usually takes advantage of (CP)FEM. Unfortunately, one single CPFEM simulation can take days to compute (Depriester et al., 2023, e.g.). Therefore, given the estimated CRSSs and the active SSs, this section provides a method to estimate the local stresses, thus allowing to avoid CPFEM (meshless approach).

For every active SS, we know that the shear stress must equal the corresponding CRSS. Hence, it is theoretically possible to infer the stress components from the CRSS of all active SSs. As the imaged surface is necessarily stress-free, we can use the plane-stress assumption:

$$\boldsymbol{\tau} = \begin{bmatrix} \sigma_{11} & \sigma_{12} & 0 \\ \sigma_{12} & \sigma_{22} & 0 \\ 0 & 0 & 0 \end{bmatrix} \tag{25}$$

For each active SS α, (3) reads:

$$\tau^\alpha = \boldsymbol{S}^\alpha : \boldsymbol{\tau} = \operatorname{sign}\left(\Delta\gamma^\alpha\right) s^\alpha \,. \tag{26}$$

Under the plane-stress assumption (25), we have:

$$\tau^\alpha = S^\alpha_{11}\sigma_{11} + S^\alpha_{22}\sigma_{22} + \left(S^\alpha_{12} + S^\alpha_{21}\right)\sigma_{12} \tag{27}$$

Let $\alpha_1, \alpha_2, \ldots, \alpha_p$ be the indices of the p active SSs. Considering only this set of SSs, combining (26) and (27) gives:

$$\begin{bmatrix} \operatorname{sign}\left(\Delta\gamma^{\alpha_1}\right) s^{\alpha_1} \\ \operatorname{sign}\left(\Delta\gamma^{\alpha_2}\right) s^{\alpha_2} \\ \vdots \\ \operatorname{sign}\left(\Delta\gamma^{\alpha_p}\right) s^{\alpha_p} \end{bmatrix} = \boldsymbol{S}^{\text{act}} \begin{bmatrix} \sigma_{11} \\ \sigma_{22} \\ \sigma_{12} \end{bmatrix} \quad \text{with } \boldsymbol{S}^{\text{act}} = \begin{bmatrix} S^{\alpha_1}_{11} & S^{\alpha_1}_{22} & S^{\alpha_1}_{12} + S^{\alpha_1}_{21} \\ S^{\alpha_2}_{11} & S^{\alpha_2}_{22} & S^{\alpha_2}_{12} + S^{\alpha_2}_{21} \\ \vdots & \vdots & \vdots \\ S^{\alpha_p}_{11} & S^{\alpha_p}_{22} & S^{\alpha_p}_{12} + S^{\alpha_p}_{21} \end{bmatrix} \tag{28}$$

Conversely, for each inactive SS β, we have:

$$-s^\beta < \tau^\beta < s^\beta \tag{29}$$

Let $\beta_1, \beta_2, \ldots, \beta_q$ be the indices of the q inactive SSs (with $p+q=N$); Eq. (29) reads:

$$\begin{bmatrix} -s^{\beta_1} \\ -s^{\beta_2} \\ \vdots \\ -s^{\beta_q} \end{bmatrix} < \boldsymbol{S}^{\text{ina}} \begin{bmatrix} \sigma_{11} \\ \sigma_{22} \\ \sigma_{12} \end{bmatrix} < \begin{bmatrix} s^{\beta_1} \\ s^{\beta_2} \\ \vdots \\ s^{\beta_q} \end{bmatrix} \quad \text{with } \boldsymbol{S}^{\text{ina}} = \begin{bmatrix} S^{\beta_1}_{11} & S^{\beta_1}_{22} & S^{\beta_1}_{12} + S^{\beta_1}_{21} \\ S^{\beta_2}_{11} & S^{\beta_2}_{22} & S^{\beta_2}_{12} + S^{\beta_2}_{21} \\ \vdots & \vdots & \vdots \\ S^{\beta_q}_{11} & S^{\beta_q}_{22} & S^{\beta_q}_{12} + S^{\beta_q}_{21} \end{bmatrix} \tag{30}$$

Hence, the components of the stress tensor can be estimated by inverting (28) while keeping (30) true. There is obviously no exact solution for this, but an approximate solution is given by the least-square criterion:

$$\begin{bmatrix} \sigma_{11} \\ \sigma_{22} \\ \sigma_{12} \end{bmatrix} \approx \underset{\boldsymbol{t}\in\mathbb{R}^3}{\operatorname{Arg\,min}} \left\{ \sum_{i=1}^{p} \left(\sum_{j=1}^{3} S^{\text{act}}_{ij} t_j - \operatorname{sign}\left(\Delta\gamma^{\alpha_i}\right) s^{\alpha_i} \right)^2 \right.$$

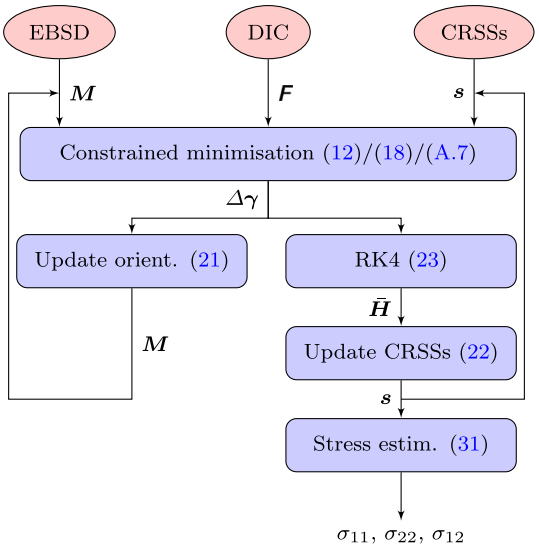

Fig. 3. Schematic representation of the proposed algorithm: for each pixel in the EBSD map and at each iteration (step), $\Delta\boldsymbol{\gamma}$ is computed first; then the crystallographic orientation ($\boldsymbol{M}$) and the CRSSs ($\boldsymbol{s}$) are updated accordingly.

$$\text{such that: } \begin{bmatrix} -s^{\beta_1} \\ -s^{\beta_2} \\ \vdots \\ -s^{\beta_q} \end{bmatrix} < \boldsymbol{S}^{\text{ina}}\boldsymbol{t} < \left. \begin{bmatrix} s^{\beta_1} \\ s^{\beta_2} \\ \vdots \\ s^{\beta_q} \end{bmatrix} \right\} \tag{31}$$

Eq. (31) is a non-linear minimisation problem with linear inequality constraints.

If $p \leq 3$, $\boldsymbol{S}^{\text{act}}$ can be singular, or close to be (ill-conditioned); in this case, the stress cannot be estimated. It is worth mentioning that numerical solving of (12) and (18) necessarily leads to all activities not exactly equal to zero although the Schmid theory states that $\Delta\gamma^\beta = 0$ if SS β is inactive. Thus, we consider here that a SS is active if its relative activity (see Section 5.2 for details) is greater than 5%, as suggested by Guery et al. (2016b).

4.5. Implementation

As a summary, Fig. 3 outlines the subsequent steps used in this paper to estimate the mechanical fields from DIC measurements, as detailed above. This whole algorithm was implemented in MATLAB®; the code is freely available online.[3] The manipulation of SSs and other crystallographic-related considerations were done with the aid of the MTEX toolbox (Bachmann et al., 2010). The non-linear optimisations with linear (in)equality constraints (12), (18) and (31) were solved with the `fmincon` function in MATLAB®.

It is worth mentioning that numerical minimisers, such as `fmincon`, usually require a first guess. For the L_1 method (12), the Moore–Penrose pseudoinverse (Goodfellow et al., 2016, Chap. 2) of $\boldsymbol{K}$ thus provides a good candidate, for it minimises its L_2-norm, whose solution is by essence close to that of the L_1 minimisation.[4]

5. Results

5.1. The L_1 vs. the Energy methods

The L_1 and the Energy methods, as detailed above, were applied on the material introduced in Section 2. The current section presents the results from both the methods.

[3] https://github.com/DorianDepriester/SSLIP-CP/

[4] This actually also applies for the Energy method (18) as both the methods lead to almost the same results (see Section 5.1).

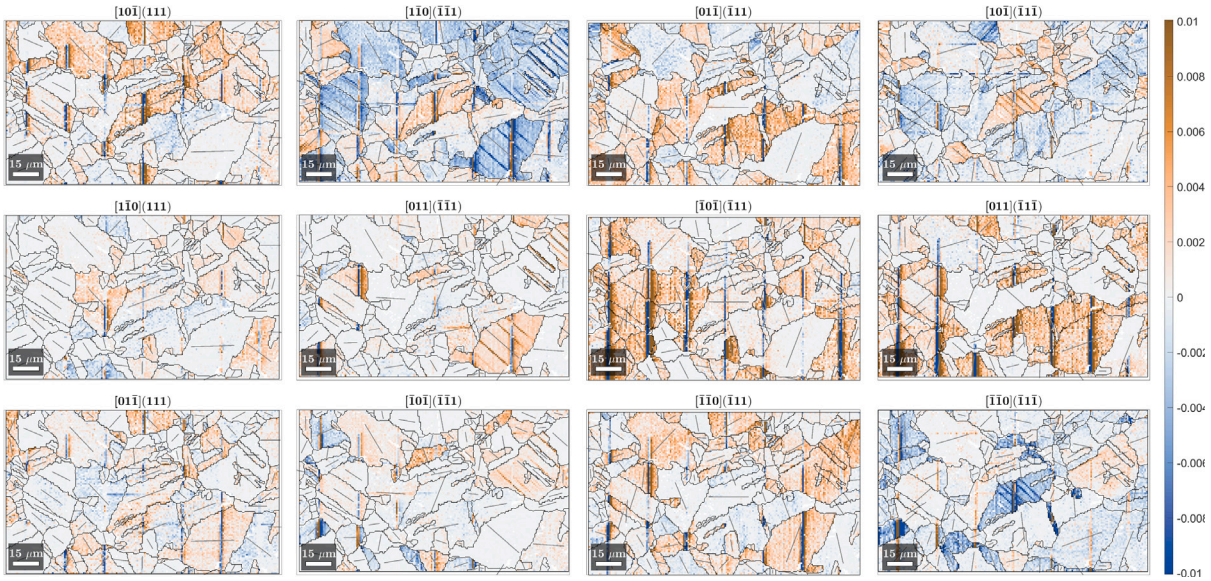

(a) Step 1

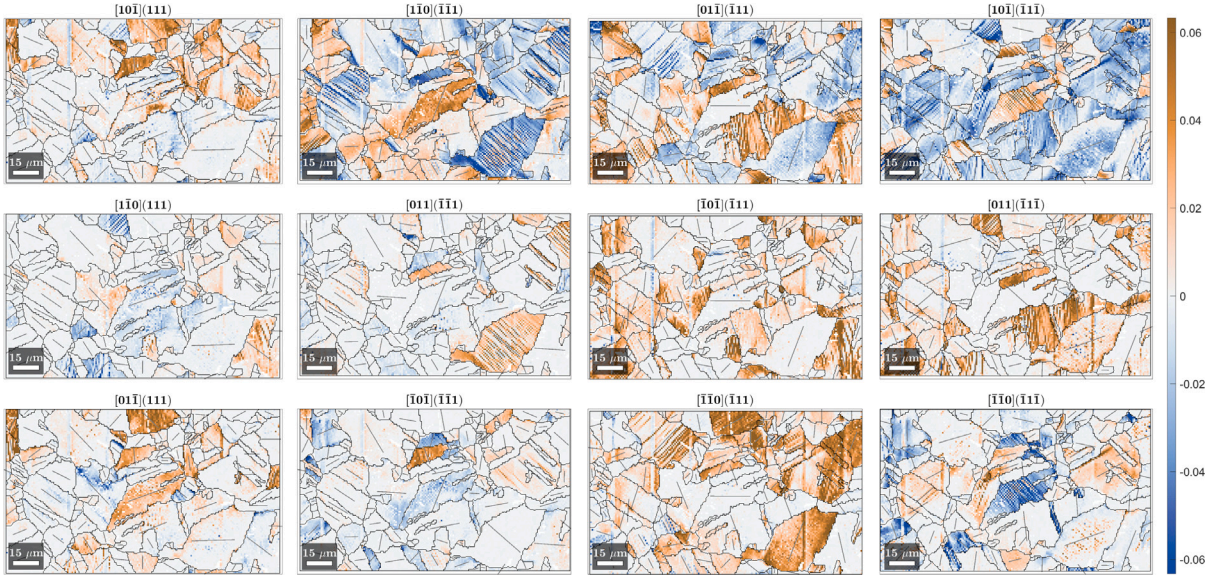

(b) Step 2

Fig. 4. Slip activities ($\Delta\gamma$) computed with the L_1 method: the straight lines illustrate the traces of the considered slip planes.

Fig. 4 illustrates the slip activity on each SS, using the gradient values shown in Fig. 2 with the L_1 method. Black lines illustrate the grain boundaries, whereas the traces of the slip bands are represented as grey lines in Fig. 4. This confirms that the intragranular shear bands, evidenced by HR-DIC, are parallel to the corresponding slip traces (see for instance the activity of $[1\bar{1}0](\bar{1}\bar{1}1)$ SS). The vertical artefacts in DIC, as reported in Section 2.2 (see Fig. 2(a)), result in the same kind of artefacts at early stages of the deformation (Fig. 4(a)). A method is proposed in Appendix A to reduce them.

Vermeij et al. (2023) reported the occurrence of cross slip in FCC Ni-based superalloy, evidenced by "kinked" bands; conversely, no such bands were evidenced here (see Fig. 4). This difference is probably due to the absence of precipitates in pure copper, as opposed to the Ni-based superalloy (Harte et al., 2020). It is also worth mentioning that slip can occur as localisation bands, as mentioned above, but also in a diffuse way (see for instance $[\bar{1}\bar{1}0]\,(\bar{1}11)$ in Fig. 4(c)); furthermore, localisation bands can occur on one SS whilst diffuse slip occurs on another SS (see for instance the slip activities for $[1\bar{1}0]\,(\bar{1}\bar{1}1)$ and $[\bar{1}\bar{1}0]\,(\bar{1}11)$ in the highlighted grain in Fig. 4(c)).

The Energy method, as detailed in Section 4.1.2, was applied on the DIC data, as illustrated in Fig. 5. For the sake of brevity, only step 3 is depicted in it. It appears that the results are very similar to those found using the L_1 method (See Fig. 4(c) for comparison). In order to provide more details about the slip activities and highlight the similarities between the two methods, Fig. 6 shows the slip activities at step 3 for the grain highlighted in blue in Fig. 1(b) only, for both the methods. This thus confirms that the differences between the two methods are barely visible. In Fig. 6, the trace of the slip plane is not always perfectly aligned with the apparent localisation band (see for instance the activity for the $[\bar{1}\bar{1}0]\,(\bar{1}1\bar{1})$ SS); this can be due to regular grid used for EBSD indexing (rastering), which could be avoided using a finer EBSD resolution. This small angle can also be due to a slight deviation between SEM imaging and EBSD acquisition (because of sample tilting for instance). Nevertheless, its seems that the misalignment here is small enough not to impair the present analyses.

Fig. 6 also confirms that slip localisation and diffuse slip can occur at once (see for instance $[\bar{1}\bar{1}0]\,(\bar{1}1\bar{1})$ and $[1\bar{1}0]\,(\bar{1}\bar{1}1)$ SSs), as reported

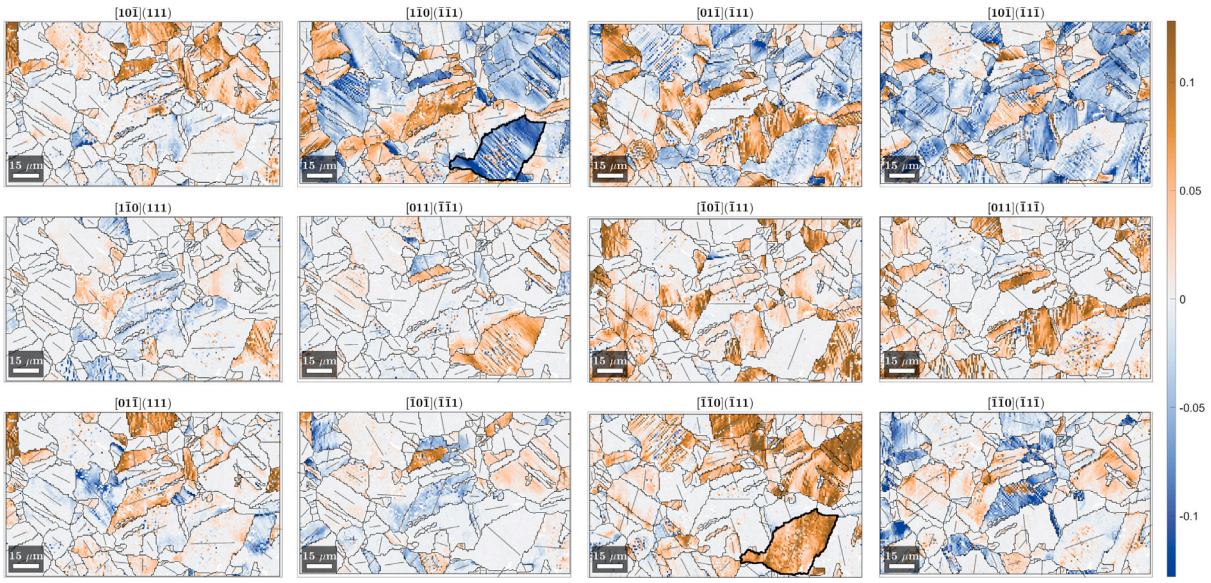

(c) Step 3

Fig. 4. (*continued*).

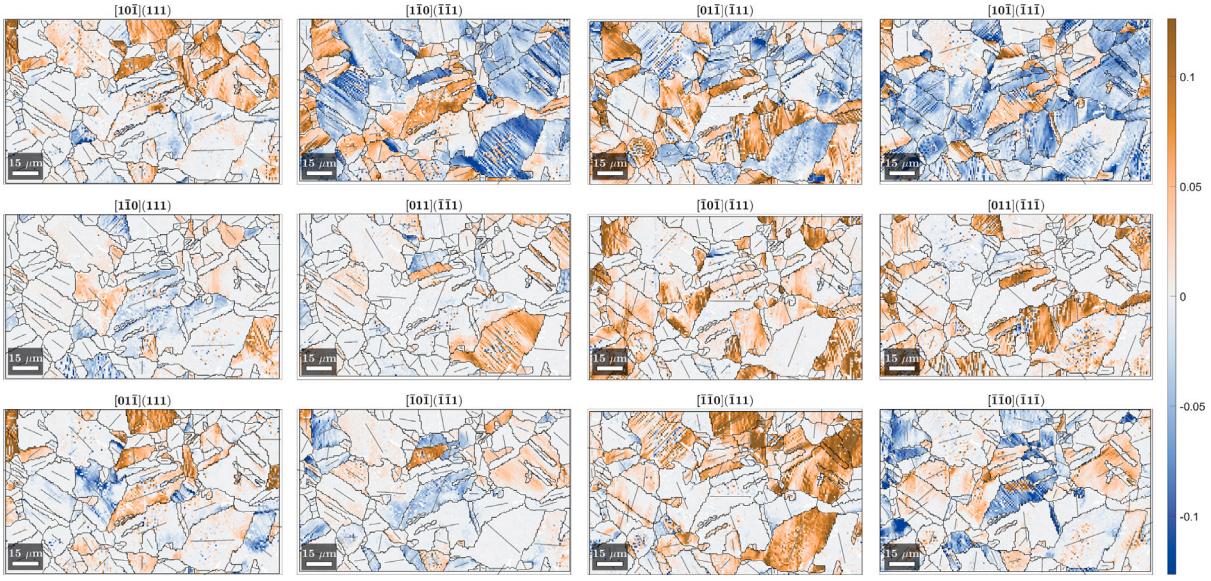

Fig. 5. Slip activities ($\Delta\gamma$) computed with the Energy method (Step 3).

above. This suggests that the analysis of localisation bands is not sufficient to fully describe the slip activity; hence the superiority of the proposed methods (as well as that of the SSLIP algorithm (Vermeij et al., 2023, 2024)) over slip trace-based methods.

In order to evidence the differences between the L_1 and the Energy methods, Fig. 7 shows the slip activities unravelled with the Energy criterion against those found using the L_1 method. In order to ensure that the stitching artefacts do not impair this analysis, efforts have been made to consider datapoints away from these artefacts only. This confirms that both the L_1 and the Energy methods are almost equivalent here. It is worth noticing that, at least, they always lead to consistent signs on $\Delta\boldsymbol{\gamma}$. Fundamental differences between the L_1 and the Energy criteria are further discussed in Section 6.1. The largest difference between the L_1 and the Energy method is reached at step 3, where work hardening plays a leading role.

In order to analyse the spatial distribution of differences between the L_1 and the Energy method, we define the L_2-norm of the relative error between the slip activity found with the L_1 method and that found with the Energy method:

$$\varepsilon = \frac{\left\| \Delta\boldsymbol{\gamma}^{L_1} - \Delta\boldsymbol{\gamma}^{\text{Energy}} \right\|_2}{\left\| \Delta\boldsymbol{\gamma}^{\text{Energy}} \right\|_2}$$

The spatial distribution of ε is illustrated in Fig. 8 for each step. It appears that no clear relationship between the location and the error can be raised, even in the stitching artefacts, as they are not visible in this figure. This means that the difference between the two methods is not related to the location (grain boundaries, twins etc.). Since the results are almost the same with both the methods, but the energy method is more realistic,[5] only the latter will be used hereafter.

In order to check that the linear constraint (9) is always satisfied, its residual, defined as the L_2-norm of the difference between left- and

[5] It will be demonstrated in Section 6.3 that it is indeed more accurate.

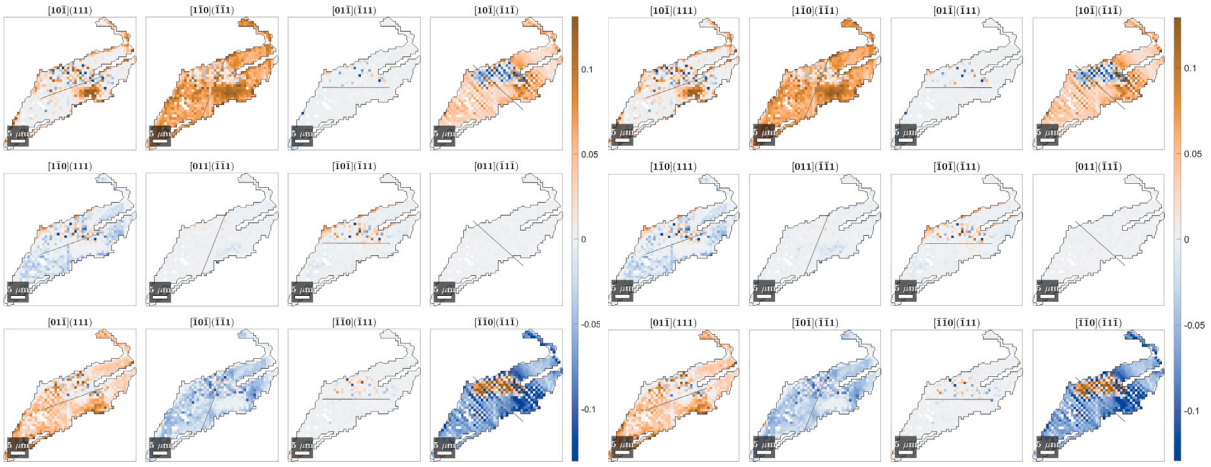

(a) L_1 (b) Energy

Fig. 6. Details of the slip activities ($\Delta\gamma$) at step 3 within the grain highlighted in blue in Fig. 1(b), depending on the method.

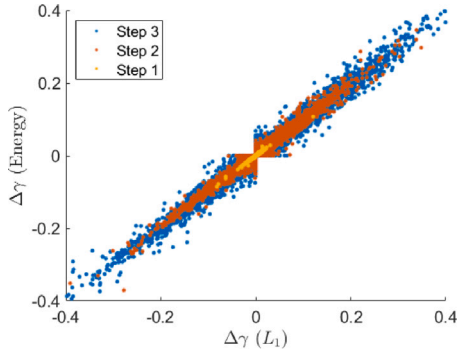

Fig. 7. Comparison between the results obtained from the L_1 and the Energy methods.

right-hand sides of (9) was computed.[6] The values of the residual, as depicted in Fig. 9, were below 1×10^{-16} for 99.9% of points. Taking into account the round-off error, this thus confirms that the equality constraint was almost always satisfied. The residual seems to increase as the deformation increases; this is because the increment of gradient ($\Delta \boldsymbol{F}$) is not constant between all the steps, as evidenced by the non-evenly spaced steps in Fig. 1(a). Similarly, the residual is higher in localisation bands because the components of $\Delta \boldsymbol{F}$ are higher at these locations (see Fig. 2).

5.2. Active slip systems

This section investigates the number of active slip systems for each datapoint (pixel) at each step.

The relative slip activity of SS α, as introduced by Guery et al. (2016b), is defined as:

$$A^\alpha = \frac{|\Delta\gamma^\alpha|}{\sum_\beta |\Delta\gamma^\beta|}$$

A^α was computed for every datapoint away from the stitching artefact. Fig. 10 shows the corresponding mean values of A^α, once sorted in descending order (see blue solid bars), whereas the minimal and maximal values are illustrated as error bars. On average, the most active SS accounts for 34% of the total slip activity. At most, 10 SSs are active (see upper error bars), whereas in some cases only 3 SSs are active (see lower error bars). The orange curve in Fig. 10 illustrates the cumulative sum of the sorted mean values. This shows that, on average, 6 SSs can be considered active at once, for they account for 95% of total slip activity. Considering that a SS α is active if $A^\alpha > 0.05$, Fig. 11 shows the histograms of the number of active SSs (denoted p in Section 4.4). The distribution of p are almost the same for all steps. This also confirms that, in most cases, 5 or 6 SSs are active at once. Conversely, Guery et al. (2016b) reported that, using the same 95% criterion, only 4 SSs were active at once in A316LN stainless steel on average. At this point, it is impossible to conclude whether this discrepancy is because of the materials (copper *vs.* austenitic steel) or the methods (DIC *vs.* CPFEM). However, it will be shown in Section 6.3 that the method was identified as the culprit. According to Fig. 11, conditions where $p = 1$ or $p > 8$ are very rarely met, since their frequencies are below 2.5×10^{-5} and 9.9×10^{-4}, respectively. Anticipating the number of active SSs (p) is a valuable clue for the optimisation task, for this knowledge could be used to reduce the size of the investigated space (denoted N above), similarly to what Vermeij et al. (2024) did.

5.3. Slip activity path

This section analyses the path followed by each SS, that is if the shear strain on each SS changes monotonously or not.

For each datapoint, Fig. 12(a) (resp. 12(b)) shows the slip activities at step 2 (resp. step 3), as functions of slip activities at step 1 (resp. step 2). Again, only datapoints away from stitching artefacts were considered here. It appears that, in general, the direction of an active SS (sign of $\Delta\gamma$) keeps constant at two subsequent steps. More precisely, 68.7% of slip activities keep the same sign between step 1 and step 2; this ratio goes to 73.7% between step 2 and step 3. This increase suggests that the strain behaviour of the grains enters a steady-state regime at step 3, as also suggested in Depriester et al. (2023). A possible implication for this is that, at this stage, the local crystallographic reorientations are sufficient to promote continuous slip activity. 55.5% of slip activities keep the same sign between steps 1, 2 and 3.

In order to highlight the spatial distribution of the aforementioned sign changes in slip activities, Fig. 13 shows, for each datapoint, the number of SSs whose activity changed sign between step 1 (resp. 2) and step 2 (resp. 3). As a result, it seems that datapoints near grain boundaries are more likely to have consistent slip orientations between successive steps.

[6] This is consistent with the distance function used by Vermeij et al. (2023) to define the inequality constraint.

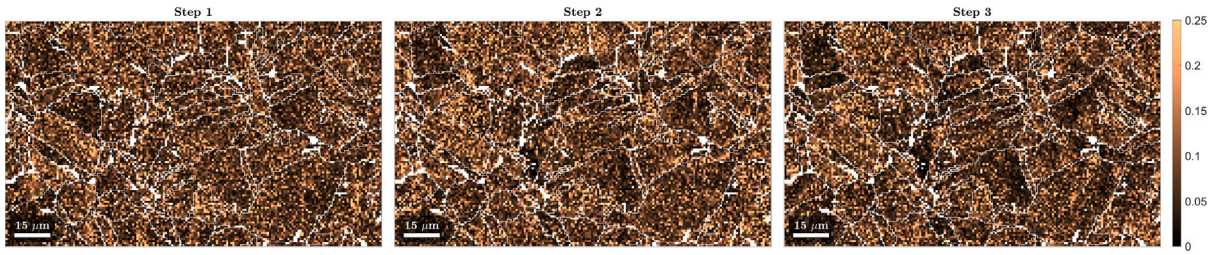

Fig. 8. Local values of the relative error in slip activities between the Energy and the L_1 method (ϵ).

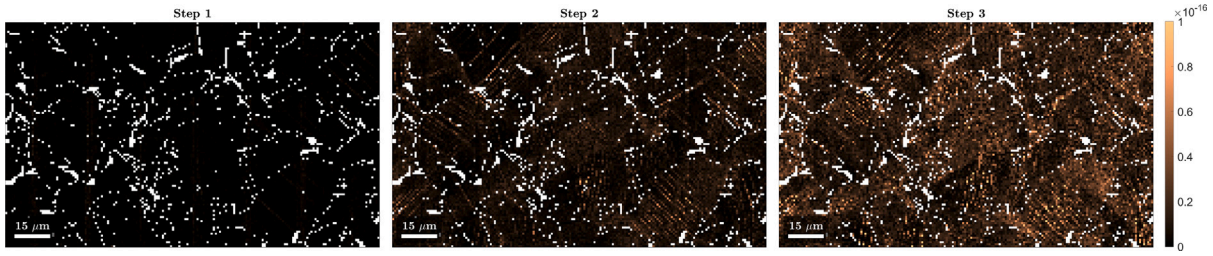

Fig. 9. Residuals of equality constraint (9), when using the Energy method.

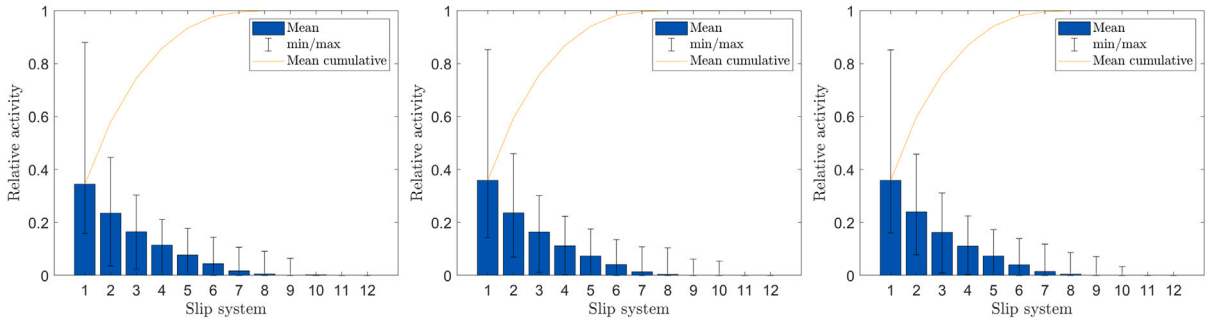

(a) Step 1 (b) Step 2 (c) Step 3

Fig. 10. Histograms of mean relative slip activities (descending order) and corresponding cumulative value (orange curve). The error bars provide the recorded extrema.

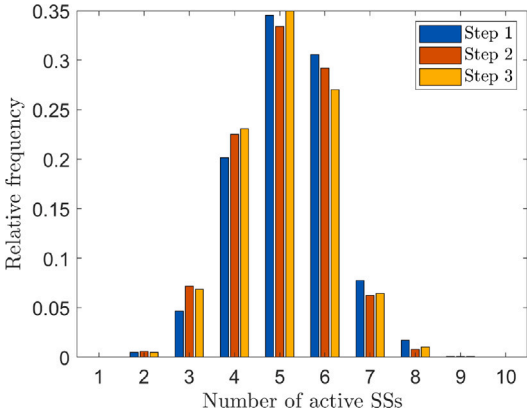

Fig. 11. Histograms of the numbers of active slip systems (p) for each step.

5.4. Validity of the Schmid theory

This section investigates if the Schmid theory, as detailed in Section 3.1, is satisfied here. First, the shear stress on each SS was computed with (2), assuming that the stress was homogeneously distributed in the polycrystal, meaning that, at local scale, the stress was equal to that applied at macroscopic level, as reported in Fig. 1(a). The reason for this hypothesis is detailed elsewhere (Goulmy et al., 2022). Fig. 14 illustrates the slip activities as functions of the corresponding resolved shear stress (τ^α). Globally, the slip activity seems to increase with the resolved the shear stress, thus validating the Schmid theory. Nevertheless, these plots appear noisy, probably because the homogeneous stress assumption mentioned above is not true everywhere. In 73.7% of cases, the sign of the slip activity was consistent with that of the shear stress, as stated in (3).

5.5. Stress estimation

The local stress was estimated through the Energy method, following the procedure described in Section 4.4. The local values of the tensile stress along the tensile direction (σ_{11}) are depicted in Fig. 15(a). These maps appear slightly noisy, specially in the stitching bands and in the localisation bands. Some values even seem unrealistic (e.g. where high compressive stress is recorded). Hence, Fig. 15(b) shows the grain-wise median value of the tensile stress. In this map, the estimated stress appears more uniformly distributed among all grains. This is consistent with the results presented in earlier works on this material (Goulmy et al., 2022; Depriester et al., 2023). The macroscopic stress was computed as the overall median of the local stresses. Fig. 1(a) shows the macroscopic tensile stress (σ_{11}) estimated at each step, whereas Table 3 provides all the components (σ_{11}, σ_{22} and σ_{12}). It is clear that the estimated tensile stress is very close to the experimental one, even though only 3 steps were used here. This accuracy is achieved

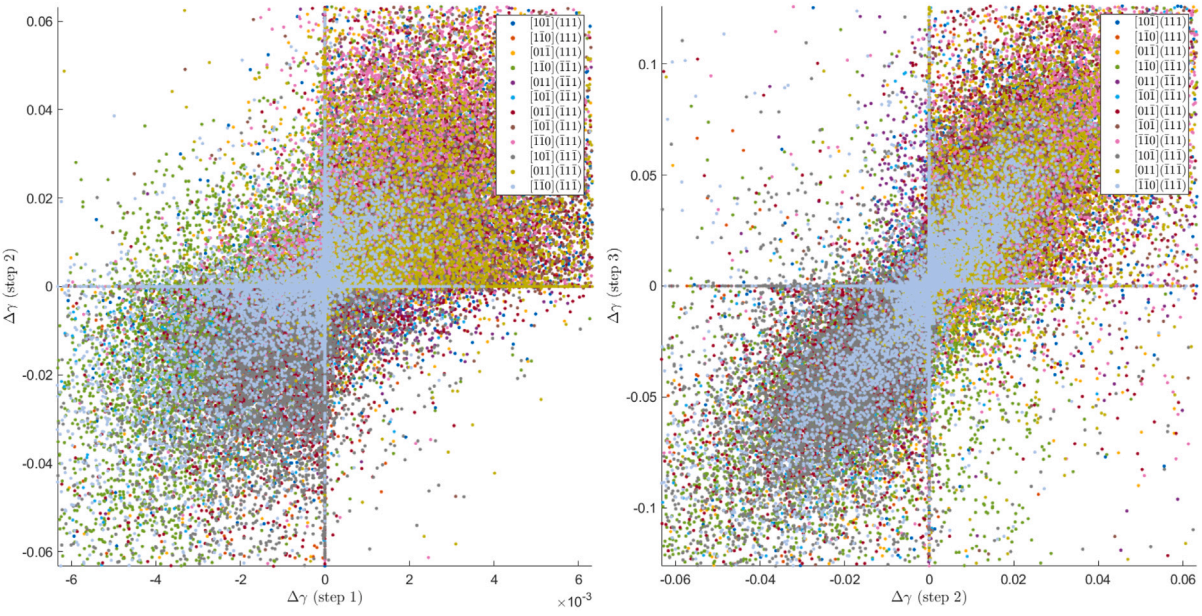

(a) Step 2 vs. step 1 (b) Step 3 vs. step 2

Fig. 12. Slip activities at a given step *vs.* those at a previous step.

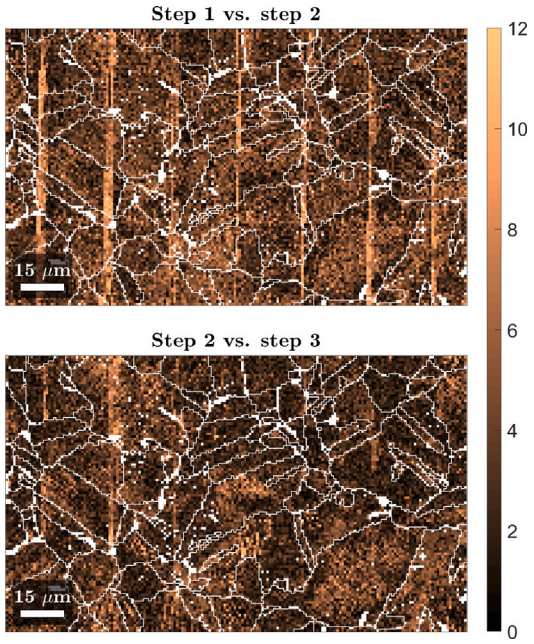

Fig. 13. Number of SSs whose activity changed mathematical sign between two successive steps. Grain boundaries are shown as white lines.

thanks to the RK4 integration scheme (22). It also appears that the estimation results in compressive stress along the transverse direction ($\sigma_{22} < 0$) at step 3, which seems unrealistic here; although it cannot be measured during the in situ tensile test, it should be close to zero.[7] This is probably because we neglect the elastic strain here; this means that the material appears "stiffer" in the proposed approach than in reality, hence an additional compressive stress to reach the same strain.

[7] CPFEM simulations show that it is actually slightly positive; see Section 6.3 for details.

Table 3
True macroscopic stress (MPa), depending on the estimation method: experimental (in situ tensile test), from DIC measurements (Section 4.4), or from CPFEM simulations (Section 6.3). Dot (·) indicates that the value cannot be estimated.

Step	Experiment	Estimated from DIC	CPFEM simulation
1	$\begin{bmatrix} 42.8 & \cdot & \cdot \\ & \cdot & \cdot \\ & & \cdot \end{bmatrix}$	$\begin{bmatrix} 44.8 & -1.13 & \cdot \\ & 9.63 & \cdot \\ & & \cdot \end{bmatrix}$	$\begin{bmatrix} 38.2 & -3.34 & 2\times10^{-4} \\ & 7.45 & 7\times10^{-5} \\ & & -6\times10^{-3} \end{bmatrix}$
2	$\begin{bmatrix} 96.0 & \cdot & \cdot \\ & \cdot & \cdot \\ & & \cdot \end{bmatrix}$	$\begin{bmatrix} 106.9 & -2.32 & \cdot \\ & 7.61 & \cdot \\ & & \cdot \end{bmatrix}$	$\begin{bmatrix} 95.8 & 1.41 & 5\times10^{-3} \\ & 17.1 & 4\times10^{-3} \\ & & -0.20 \end{bmatrix}$
3	$\begin{bmatrix} 166.5 & \cdot & \cdot \\ & \cdot & \cdot \\ & & \cdot \end{bmatrix}$	$\begin{bmatrix} 169.9 & -0.24 & \cdot \\ & -17.3 & \cdot \\ & & \cdot \end{bmatrix}$	$\begin{bmatrix} 171.0 & 2.11 & -9\times10^{-3} \\ & 27.0 & 0.02 \\ & & -1.34 \end{bmatrix}$

It is worth mentioning that the method used in this paper to estimate the local stress does not take advantage of the balance of linear momentum equation. Therefore, a possible improvement is to regularise the stress field so that the aforementioned equation is satisfied. In addition, no neighbouring effect is considered here, although it is well known that plastic incompatibilities can induce stress concentration near GBs (Salvini et al., 2024, and references therein), potentially resulting in elastic strain. The material used in the present work is soft enough to neglect the elastic strain Depriester et al. (2023), but a possible improvement of the proposed method is to take into account the plastic incompatibilities.

6. Discussion

6.1. 3D representation of L_1 and Energy methods

It was shown in Section 5.1 that the L_1 and the Energy methods lead to almost the same results on pure copper. Thus, this section aims at evidencing the fundamental differences between those methods.

Fig. 16 schematically illustrates the L_1-norm and the Energy function (17) in a virtual 3-dimensional space $(\gamma^1, \gamma^2, \gamma^3)$. The isovalue surface of L_1-norm is a regular octahedron (Fig. 16(a)), whereas that for the energy function is a concave octahedron (Figs. 16(c) and 16(d)). Minimising one of these functions such that (9) holds consists in

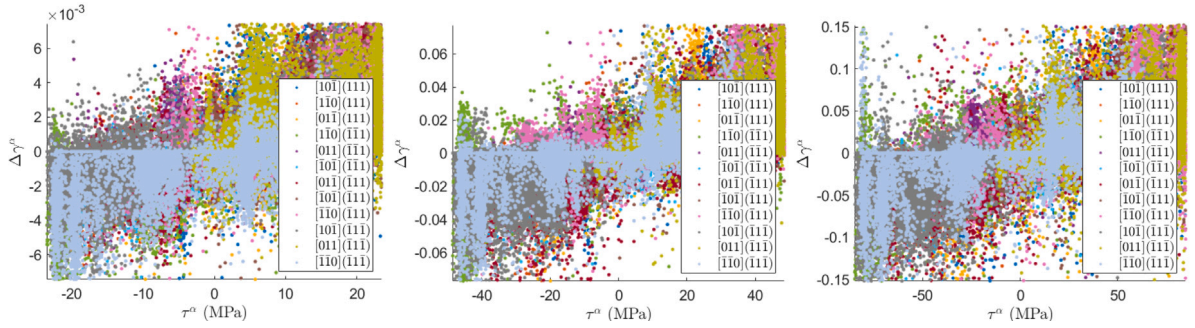

(a) Step 1 (b) Step 2 (c) Step 3

Fig. 14. Slip activities of each SS, as functions of the corresponding shear stress (τ^α). Only datapoints away from the stitching artefacts were used.

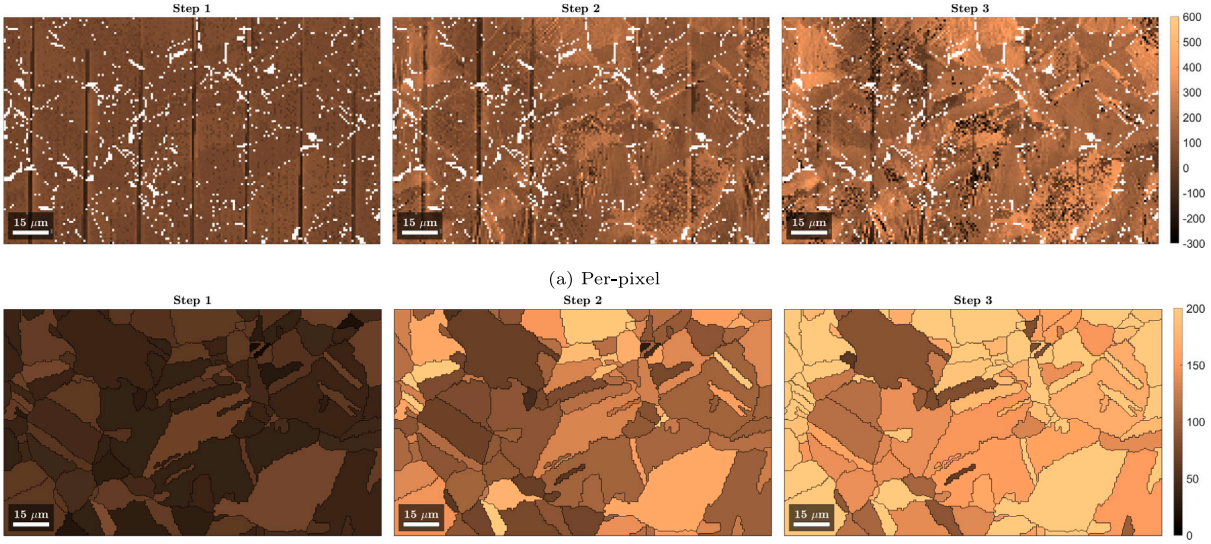

(a) Per-pixel

(b) Grain-wise median

Fig. 15. Estimated tensile stress (σ_{11}, in MPa). White region indicates that the stress could not be estimated ($\boldsymbol{S}^{\text{act}}$ is ill-conditioned).

finding the smallest octahedron tangent to the subspace defined by (9) (represented as a straight line in the 3D space of Fig. 16). It is clear that in most cases, the minimum value will be reached at the edges of the octahedrons, leading to very similar results, regardless of the function to be minimised. However, in certain circumstances, the results can be quite different, as evidenced by the location of the blue dots in Fig. 16.

As evidenced by Figs. 16(c) and 16(d), the larger q, the more concave the octahedron; and the Energy method with $q = 1$ (Fig. 16(b)) is equivalent to the L_1. One can also demonstrate that $s_0 = 0$ and $q = 0$ leads to L_2-minimisation (the octahedron becomes a sphere). As a reminder, we used $q = 1.702$, $h_0 = 309.5\,\text{MPa}$ and $s_0 = 12.22\,\text{MPa}$ here (see Table 1 for details); therefore, this explains why the L_1 and Energy methods lead to slight differences in the case of pure copper. On a more anisotropic material (e.g. HCP material), one may expect larger differences. For instance, different CRSSs correspond to different scale factors of the concave octahedrons along the three directions of Fig. 16.

6.2. Influence of the DIC window size

The aim of the section is to study the influence of the DIC resolution on the grain-wise mean and spread activities found through the proposed method.

As recalled in Section 2.2, the DIC resolution is usually defined by the window size φ. As a reminder, all the results presented above were obtained with $\varphi = 1.3\,\mu\text{m}$. This value was demonstrated to be the best compromise to evidence localisation bands with limited noise (Goulmy et al., 2022); therefore, it will be considered as the reference value hereafter.

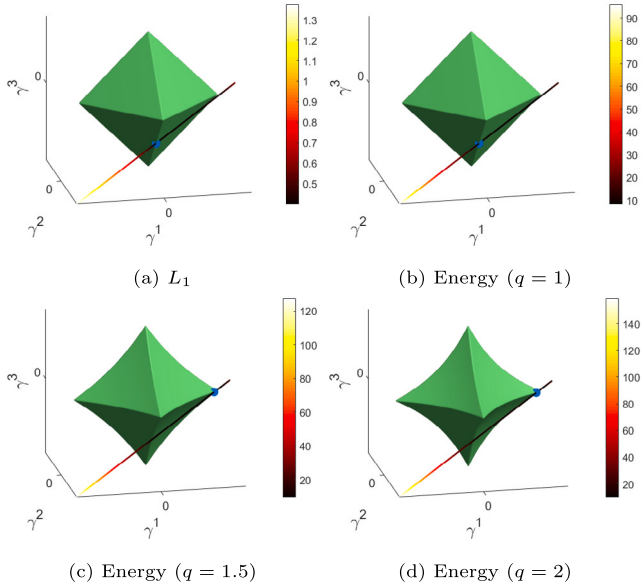

(a) L_1 (b) Energy ($q = 1$)

(c) Energy ($q = 1.5$) (d) Energy ($q = 2$)

Fig. 16. 3D representation of the minimised function: in 3D space $(\gamma^1, \gamma^2, \gamma^3)$, the straight line illustrates the subspace defined by linear equality constraint (9). It is coloured depending on the criterion (L_1 or Energy, see colourbars), whereas the blue dots show the locations of minima. The green surfaces illustrate the corresponding isovalue of this criterion in the 3D space. Figs. (b) to (d) were drawn with $h_0 = 100$ and $s_0 = 1$.

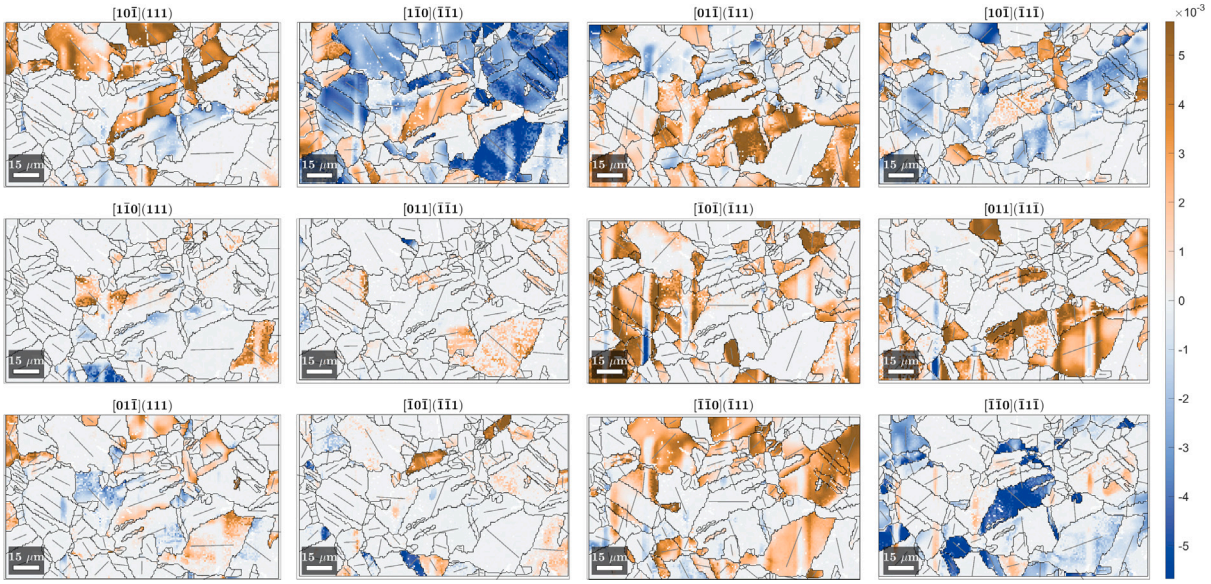

(a) Step 1

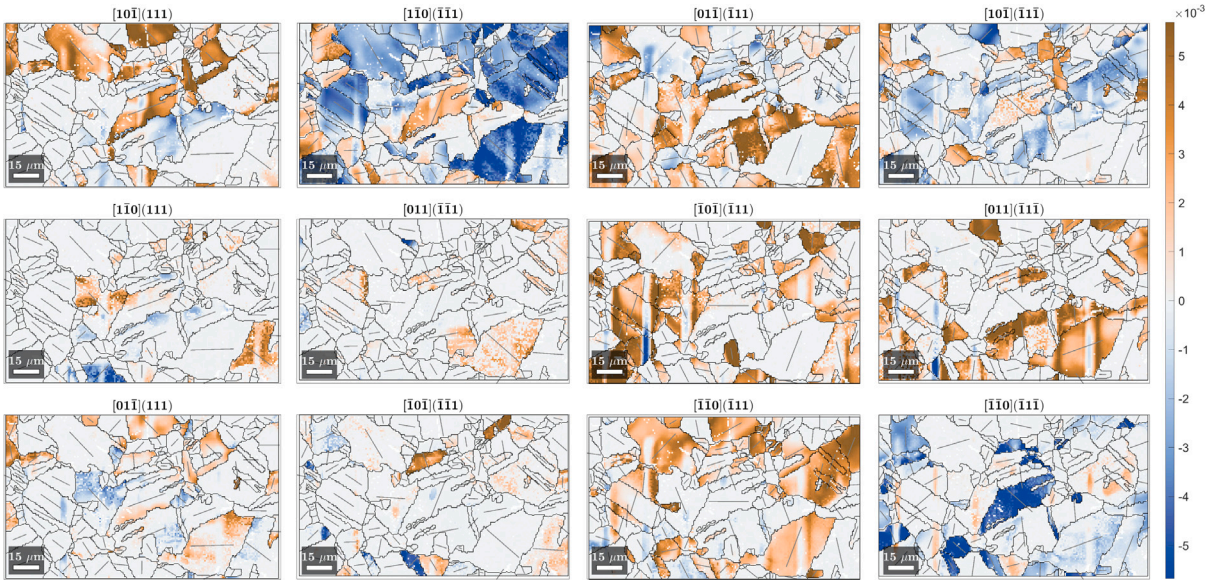

(b) Step 2

Fig. 17. Slip activities, computed from DIC measurements made with $\varphi = 9.6\,\mu m$.

The Energy method was applied with $\varphi = 5.2$, 9.6 and 25 μm. Fig. 17 illustrates the results with $\varphi = 9.6\,\mu m$.

It appears that the distribution of slip activities is similar to that found with $\varphi = 1.3\,\mu m$ (see Fig. 5 for comparison), although it is more uniformly distributed within each grain. In order to study the influence of the window size on the grain-wise distribution of slip activities, let $E(\varphi)$ and $\sigma(\varphi)$ be the grain-wise mean and the grain-wise standard deviation of slip activities found for a given window size φ, respectively. Then, let ϵ^E (resp. ϵ^σ) be the relative error between $E(\varphi)$ and $E(1.3\,\mu m)$ (resp. $\sigma(\varphi)$ and $\sigma(1.3\,\mu m)$), so that:

$$\epsilon^E(\varphi) = \frac{E(\varphi) - E(1.3\,\mu m)}{E(1.3\,\mu m)} \tag{32a}$$

$$\epsilon^\sigma(\varphi) = \frac{\sigma(\varphi) - \sigma(1.3\,\mu m)}{\sigma(1.3\,\mu m)} \tag{32b}$$

Fig. 18 (top) illustrates ϵ^E for the three window sizes, as functions of the inverse of grain size (equivalent diameter, denoted d below). It appears that, for a given window size, the spread increases roughly linearly as a function of d^{-1}; and this spread also increases as the window size increases. The dashed lines illustrates the envelope covering 68% of values (±1std) of ϵ^E, defined as:

$$\frac{-k}{d} \le \epsilon^E(\varphi) \le \frac{k}{d}$$

The values of k are provided in Fig. 19 as a function of φ.

Fig. 18 (bottom) illustrates the relative error on the grain-wise distribution spread (ϵ^σ) as a function of d^{-1}. It is clear that the standard deviation is almost always underestimated, up to a factor of two ($\epsilon^\sigma = -1$). The mean values of ϵ^σ (denoted $\bar{\epsilon}^\sigma$ below) are illustrated as dashed lines in these plots, whereas they are drawn as functions of φ in Fig. 19. Linear regressions of k and $\bar{\epsilon}^\sigma$, as depicted in Fig. 19, leads to:

$$k \approx 0.164\varphi \tag{33a}$$

$$\bar{\epsilon}^\sigma \approx -0.248\varphi \tag{33b}$$

Therefore, (33a) can be used to estimate the uncertainty on the grain-wise mean slip activity at 68% significance level, based on the window size and the grain size, whereas (33b) can be used to correct the grain-wise spread (standard deviation). This allows to use larger window

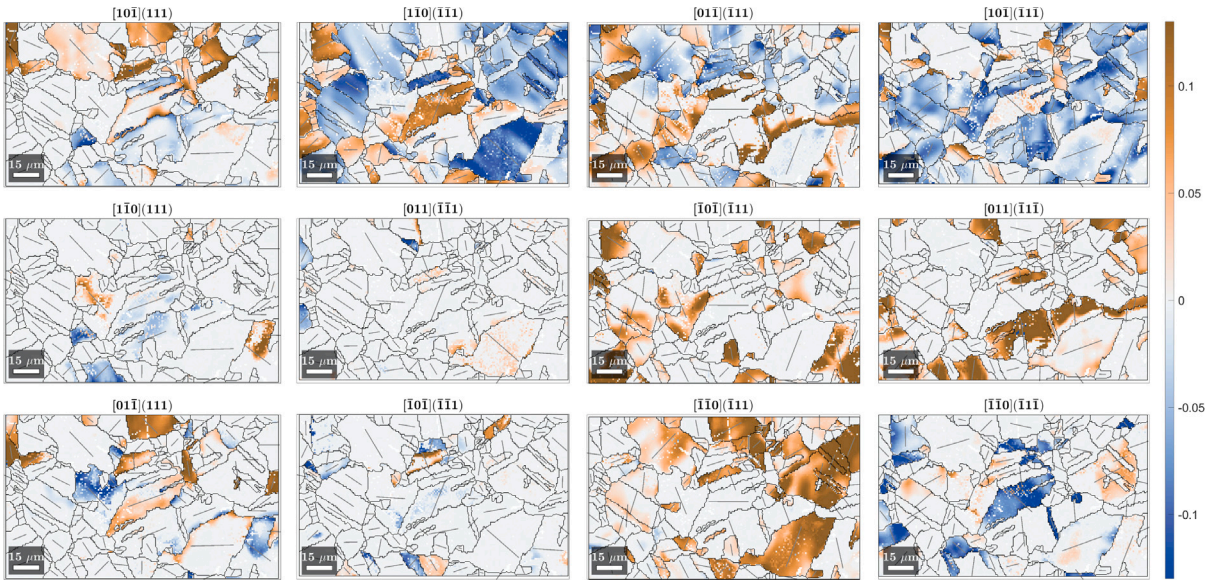

(c) Step 3

Fig. 17. (*continued*).

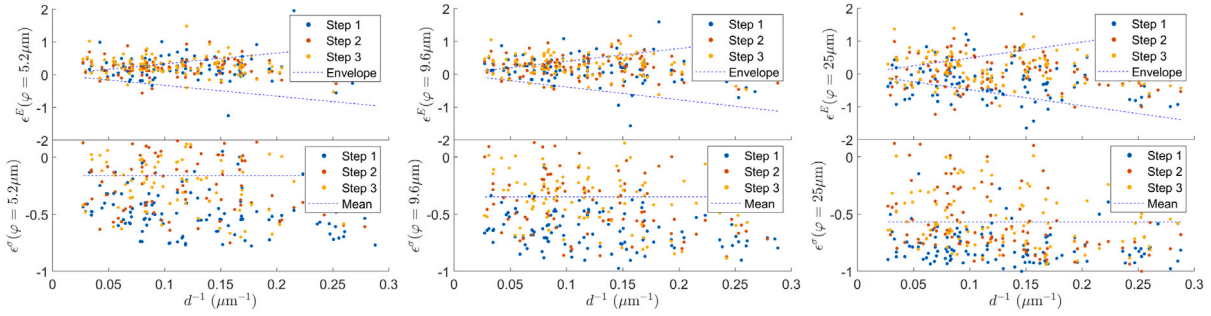

(a) $\varphi = 5.2\,\mu$m (b) $\varphi = 9.6\,\mu$m (c) $\varphi = 25\,\mu$m

Fig. 18. Relative errors on the mean values and standard deviations of grain-wise distribution of slip activities (32), depending on the inverse of the grain size.

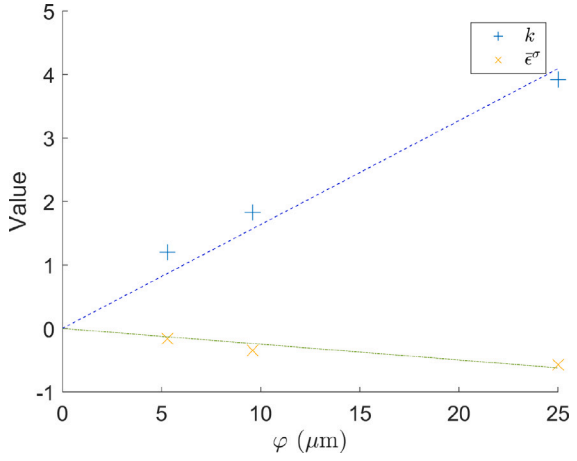

Fig. 19. Slopes of the envelope of ϵ^E (k) and mean values of ϵ^σ ($\bar{\epsilon}^\sigma$) as functions of the window size. The dashed and the dash-dotted line show the linear regressions (33) on k and $\bar{\epsilon}^\sigma$, respectively.

sizes in DIC, thus a faster SEM acquisition, a reduced noise, and a faster DIC computation. To conclude, if one wants the estimate the slip activities at mesoscopic scale (e.g., to analyse which SSs are the most active in a polycrystalline aggregate), larger window size would be enough. Conversely, smaller window sizes are required if one wants to investigate the slip activities at very local scales (e.g., for slip transmission analysis or to study strain incompatibilities (Salvini et al., 2024, e.g.)). Even though the localisation bands are not visible with bare eyes when using larger window sizes, it was demonstrated in this section that the proposed algorithm is able to provide valuable statistics about the slip activities.

6.3. Comparison with CPFEM simulations

In this section, CPFEM is used to assess the L_1 and the Energy methods, and results from DIC are compared against CPFEM simulations.

A CPFEM simulation of the in situ tensile test was performed with the PRISMS-Plasticity software (Yaghoobi et al., 2019). Prior to this simulation, the mesh conforming the grains was generated from EBSD data (see Fig. 1(b)) using the MTEX2Gmsh software (Depriester and Kubler, 2020). Experimental displacements, measured by DIC on the border of the RoI, were used as boundary conditions on the outer edges of the mesh. The material parameters were taken from Depriester et al. (2023), as recalled in Table 1. The mesh was one-element thick, and the bottom surface (in depth) and the top (imaged) were free, leading to near-plane-stress condition.

The simulated tensile curve is illustrated in Fig. 1(a), whereas all the simulated macroscopic stress components are provided in Table 3

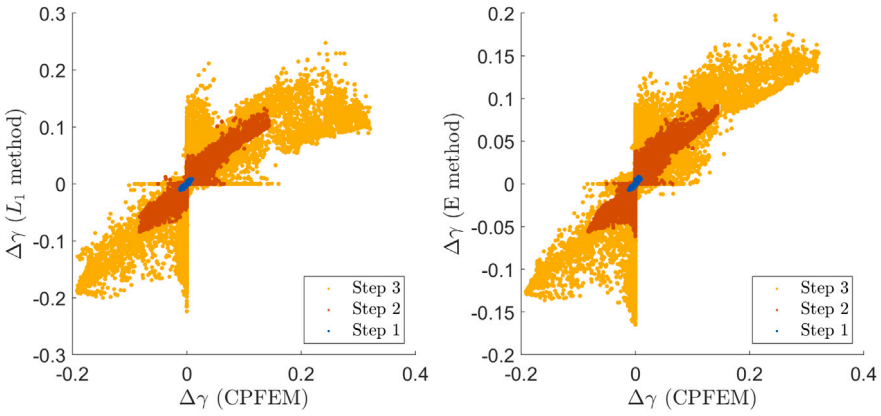

(a) L_1 method (b) Energy method

Fig. 20. Differences between the slip activities computed by CPFEM and those retrieved when applying the L_1 method (a) or the Energy method (b) on the gradient provided by CPFEM.

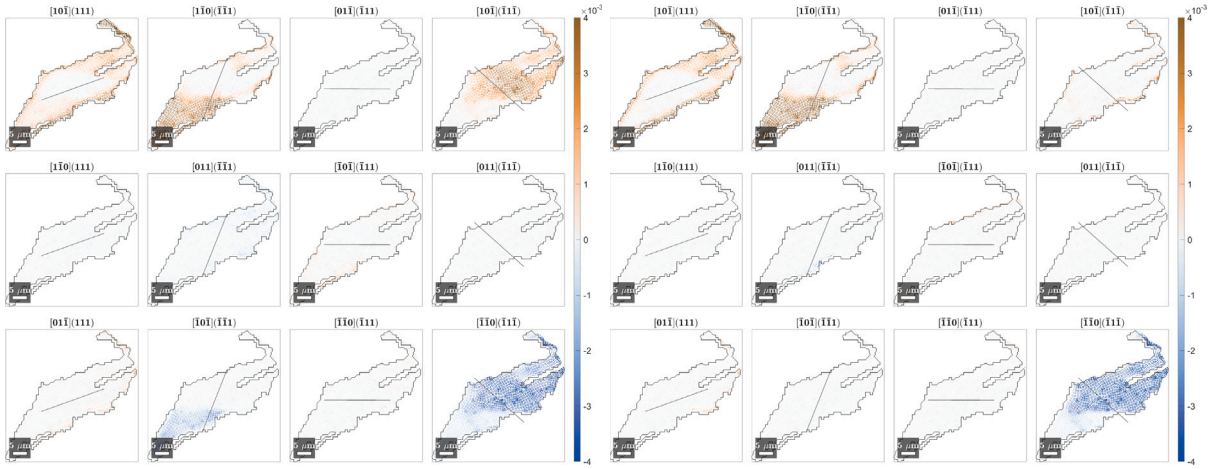

(a) Retrieved from gradient (b) As simulated

Fig. 21. Slip activities unravelled using the Energy method applied on the gradient tensor provided by CPFEM (a) or directly given by CPFEM (b). Step 1 in the grain highlighted in blue in Fig. 1(b) only.

for each step. It is clear that the plane stress assumption (25) is almost true in CPFEM, but the material also undergoes a tensile stress along the transverse direction ($\sigma_{22} > 0$). This indicates that the meshed region is smaller than the Representative Elementary Volume (REV) as it is influenced by grains outside it; otherwise, the stress would be the same as at macroscopic scale. This also confirms that σ_{22} is not accurately estimated from DIC (see Section 5.5).

In order to assess the L_1 and the Energy methods and compare the corresponding results against ground truth data, the L_1 and the Energy method were applied on the gradients given by CPFEM. The results are illustrated in Fig. 20. This confirms that both the methods are almost equivalent at steps 1 and 2, but the Energy method provides better results at step 3. This may be because strain hardening can no longer be neglected at larger strain. However, in some cases, both the methods seem to fail to *unfold* the gradient and retrieve the slip activities. In order to highlight such cases, Fig. 21(a) shows the results from the Energy method, on one single grain only (that highlighted in blue in Fig. 1(b)) at the first step. For the sake of comparison, the simulated slip activity (directly given by CPFEM) is depicted in Fig. 21(b). This proves that the proposed algorithm works well in this case for all SSs, except $[\bar{1}0\bar{1}](\bar{1}\bar{1}1)$ and $[10\bar{1}](\bar{1}1\bar{1})$, where the activity seems overestimated. This may be because of a non-monotonous activity between the reference state and step 1, which breaks the hypothesis made at (14). This is consistent with the results presented in Section 5.3, where we showed that the slip activity can change its sign. This can also be due to elastic strain, which is neglected in the Energy method, but considered in CPFEM.

Fig. 22 illustrates the grain-wise mean activity at each step, given by the CPFEM results. Theses maps are very similar to the experimental ones, specially those found with larger window size ($\varphi = 9.6\,\mu m$, see Fig. 17). This suggests that the slip activity computed from DIC with the proposed algorithm is consistent with that found by CPFEM. It is worth reminding that CPFEM is usually enable to simulate slip localisation, mainly because the element size is usually larger than the band thickness (here, the thickness of the localisation bands was 100 nm to 200 nm (Goulmy et al., 2022) whereas the element size was about 2 µm), but also because simulating such instability would require special numerical techniques (Githens et al., 2020). Therefore, larger window sizes may be sufficient if one wants to compare DIC-based slip activity estimations against CPFEM. A possible application for this is to calibrate CP parameters through an inverse analysis based on the slip activity.

In order to help comparing CPFEM results with those found by DIC, the grain-wise mean activities found by CPFEM are plotted against the corresponding value found by DIC in Fig. 23. It is clear that the overall trend is good (good consistency between CPFEM and the proposed algorithm), specially about the sign of activities, although there are some discrepancies. Indeed, for some grains, DIC measurements indicate that

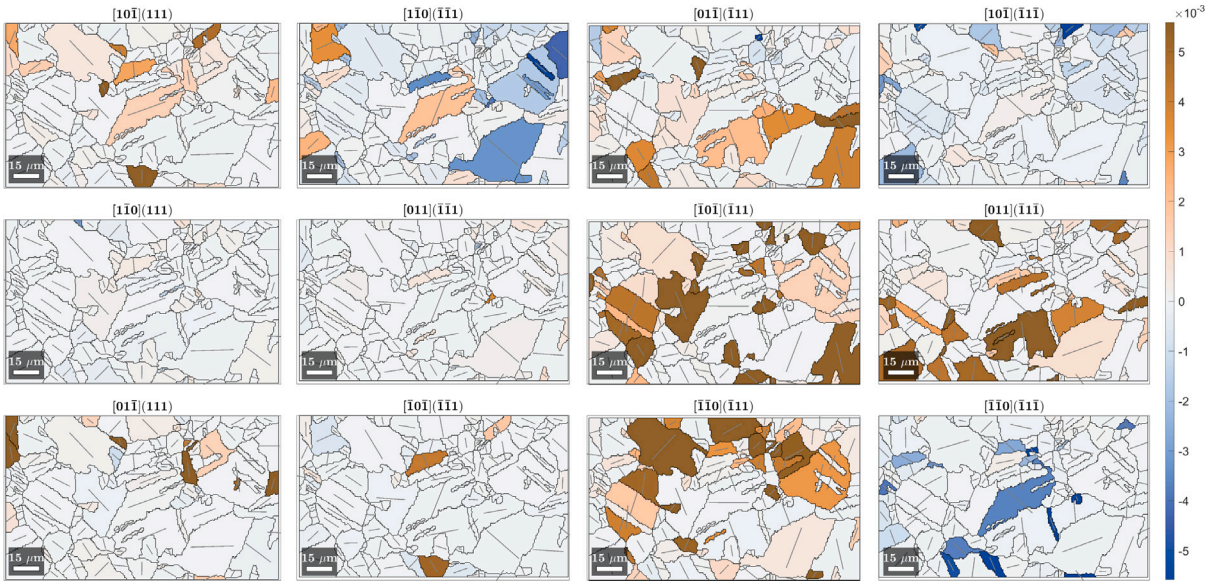

(a) Step 1

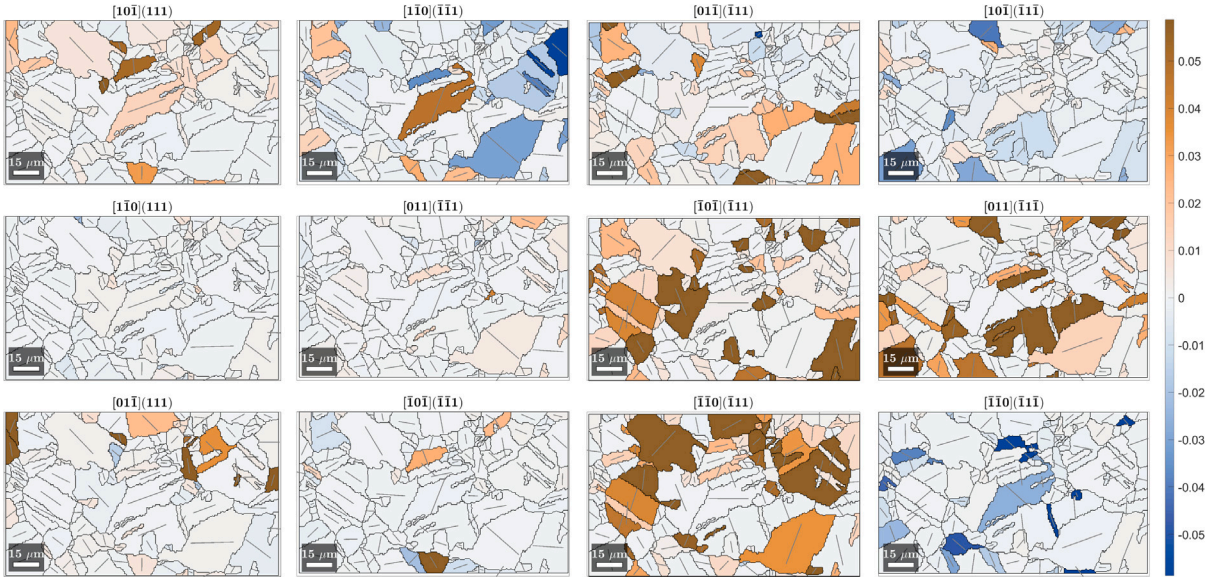

(b) Step 2

Fig. 22. Grain-wise mean slip activities, estimated from CPFEM simulations.

some plastic systems are active whereas CPFEM suggests that they are not (see the nearly "horizontal trend" in Fig. 23). This can be because of interferences with grains underneath the apparent surface, which are not taken into account in the simulation (Githens et al., 2020; Depriester et al., 2023). Conversely, Guery et al. (2016b) reported that, is some cases, CPFEM suggested some activity on SSs that were inactive according to DIC; they concluded that this error can be due to inaccuracy of the constitutive laws. Nevertheless, Guery et al. used the trace method to reach this conclusion, so they could have missed diffuse slip, which can only be evidenced with approaches similar to SSLIP, as proposed in this paper. The linear regression from the data presented in Fig. 23, weighted by the grain area (see the dashed line in this figure), demonstrates that, on average, the absolute value of slip activity is 10% smaller in CPFEM than in experiments.

Fig. 24 shows the histograms of the number of active SSs in CPFEM results (according to the 5% relative activity rule, as detailed in Section 5.2). It appears that, in most cases, only 4 SSs are actives at once in CPFEM results. This is consistent with the analysis performed by Guery et al. (2016b) on austenitic stainless steel. Conversely, the distributions illustrated in Fig. 24 are very different from the experimental ones (see Fig. 11 for comparison). This suggests that CPFEM always underestimates the number of active SSs. These differences are consistent with the difference in stress estimation reported above.

Fig. 25 illustrates the grain-wise mean tensile stress (σ_{11}), as given by CPFEM. This figure shows that the grain-wise mean stresses are close to those found from DIC (see Fig. 15(b) for comparison) for step 1 and 2. Conversely, the estimated stress seems quite different at step 3. This is probably because the slip activity estimated from the Energy method is too far from that simulated by CPFEM.

6.4. Computational performances

Vermeij et al. (2023) mentioned that `fmincon` was somehow slow for solving (12). For all the methods proposed in this paper $-L_1$, Energy and the Energy with noise reduction (not used in this paper, but detailed in Appendix A)– one can estimate the analytical expressions for

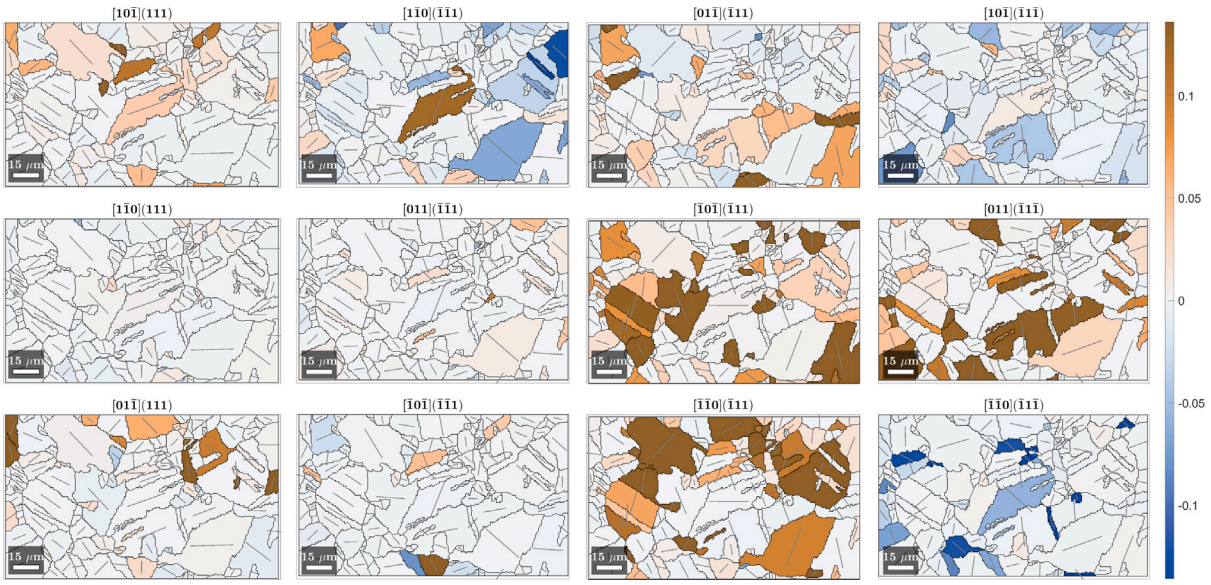

(c) Step 3

Fig. 22. (*continued*).

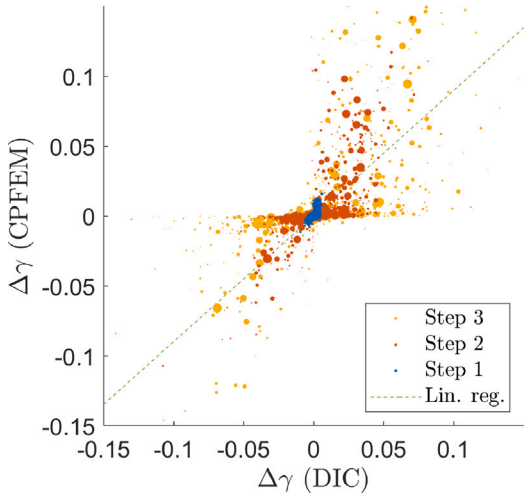

Fig. 23. Grain-wise mean activities computed from CPFEM *vs.* mean activities estimated from DIC (through the Energy method with $\varphi = 1.3\,\mu\text{m}$). The dot sizes are proportional to the grain areas.

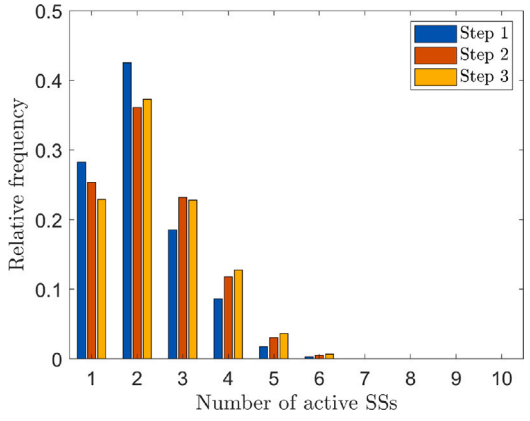

Fig. 24. Histograms of the numbers of active slip systems (p) for each step, computed from CPFEM.

Table 4
Average per-pixel running times for optimisations, depending whether the gradients and the Hessian are provided to the minimiser or not.

Method	L_1	Energy	Energy
Type of constraint	Lin. eq.[a]	Lin. eq.[b]	Non lin. ineq.[c]
No gradient nor Hessian	0.219 s	0.237 s	8.87 s
Gradient provided, no Hessian	0.217 s	0.200 s	2.41 s
Gradient and Hessian provided	0.118 s	0.101 s	0.86 s

[a] Eq. (12).
[b] Eq. (18).
[c] Eq. (A.7).

the gradients and Hessians of the minimised functions (see Appendix B for details). Providing them to the minimiser (`fmincon` here) avoids using finite differences to estimate them, thus usually resulting in a faster convergence. Table 4 gives the average per-pixel running time for each method, depending on whether the gradient and the Hessian are provided to the minimiser or not.[8] It appears that for linear equality constraints, providing the gradient and the Hessian roughly speeds up the optimisation by a factor of two. For non linear inequality constraints, as done in (A.7), the optimisation is about 10 times faster. Note that all the proposed methods work per pixel, hence they can easily be parallelised (e.g. using the `parfor` function in MATLAB®).

7. Conclusion

An algorithm, inspired by that proposed by Vermeij et al. (2023), was used to estimate the plastic slip activity from in situ DIC measurements. It takes into account the following phenomena:

- incremental straining,
- hardening evolution laws,
- crystallographic reorientation during straining.

Two methods were proposed, namely the L_1 and the Energy methods. The former uses the same criterion as that proposed by Vermeij et al., but the constraints were changed, and the implementation was

[8] Tested on an Intel® Core™ i9-9880H CPU @ 2.30 GHz.

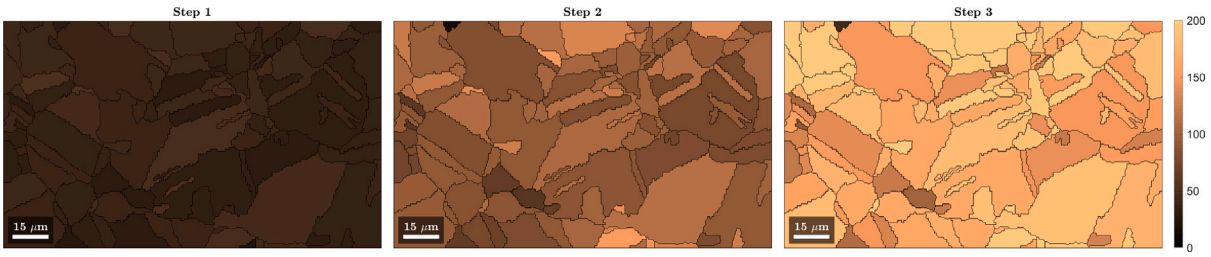

Fig. 25. Grain-wise mean values of the tensile stress (σ_{11}, in MPa) computed by CPFEM.

improved to comply with the aforementioned requirements. The Energy method is based on the dissipated plastic energy, with the same constraints as for the L_1 method. They successfully unravel the slip activities, whether the latter are localised or diffuse. In this work, both the methods almost lead to the same results, but they should differ for more anisotropic materials (with non-cubic symmetry); work in this direction is underway by the present authors and will be the subject of another publication. The Energy method is more accurate, specially at larger strain, as the optimisation criterion is more realistic. Nevertheless, it requires to fully describe the hardening evolution laws, which is usually not straightforward (Depriester et al., 2023).

Based on the aforementioned evolution laws and the records of slip activities, it was shown that the tensile stress could be estimated at macroscopic and grain scales with about 10% accuracy, even with a limited number of increments.

The influence of DIC resolution was investigated. It was shown that the larger the grain, the more accurate we are when characterising the distribution of plastic activities within each grain. A set of "correction equations" were provided for smaller grains.

The results were validated by CPFEM simulations, showing good consistency in terms of active SS. However, it was shown that CPFEM usually underestimates the number of active SSs: on average, 4 SSs were active at once in CPFEM, whereas this number was evidenced to be 5 or 6 in HR-DIC.

In a future work, the elastic strain could be taken into account, but this would require special numerical techniques, as the elastic and plastic gradients are coupled in this case. Alternatively, High-Resolution EBSD (HR-EBSD) could be used to estimate the stress at grain scale.

CRediT authorship contribution statement

Dorian Depriester: Writing – review & editing, Writing – original draft, Visualization, Validation, Software, Methodology, Investigation, Formal analysis, Conceptualization. **Jean-patrick Goulmy:** Writing – review & editing, Writing – original draft, Validation, Resources, Investigation, Data curation. **Laurent Barrallier:** Writing – review & editing, Writing – original draft, Resources.

Declaration of competing interest

The authors declare that they have no known competing financial interests or personal relationships that could have appeared to influence the work reported in this paper.

Code and data availability

The MATLAB® code for the present work is available under the MIT licence on GitHub: https://github.com/DorianDepriester/SSLIP-CP/. It comes with all necessary materials (EBSD map and DIC measurements) required to replicate the results presented in the present paper.

Acknowledgements

Most of the figures in the present paper use the colour-blind-compatible colourmap "lbmap", originally proposed by Light and Bartlein (2004) and implemented in MATLAB® by Robert Demis.[9]

Appendix A. Toward a noise-independent criterion

The aim of this section is to propose a method to make the proposed algorithm robust against noise, mainly in order to remove the stitching artefacts (see Fig. 4(a) for instance). Although it is not used in this present work, the section provides the mathematical developments for future works.

We assume that when measuring the values of $\boldsymbol{F}$, a random noise $\boldsymbol{\epsilon}$ adds, such that:

$$\mathring{\boldsymbol{F}}(x,y) = \boldsymbol{F}(x,y) + \boldsymbol{\epsilon}(x,y) \tag{A.1}$$

where $\mathring{\boldsymbol{F}}$ denotes the noised gradient tensor measure. We assume that $\boldsymbol{\epsilon}$ follows a multivariate normal distribution of 2nd order random tensors, whose mean ($\boldsymbol{\mu}$) and covariance ($\boldsymbol{\sigma}$) may depend on the (x,y) coordinates, that is:

$$\boldsymbol{\epsilon}(x,y) \sim \mathcal{N}\left(\boldsymbol{\mu}(x,y), \boldsymbol{\sigma}(x,y)\right) \tag{A.2}$$

Let $\boldsymbol{f}$ be a tensorial function, defined as follows:

$$\boldsymbol{f}(\boldsymbol{g}) = \Delta\mathring{\boldsymbol{F}} - \sum_\alpha g_\alpha \boldsymbol{S}^\alpha \cdot \mathring{\boldsymbol{F}}^\theta \tag{A.3}$$

According to (A.1) and (7), we have:

$$\begin{aligned}\boldsymbol{f}(\Delta\boldsymbol{\gamma}) &= \Delta\boldsymbol{F} + \boldsymbol{Z} - \sum_\alpha \Delta\gamma^\alpha \boldsymbol{S}^\alpha \cdot (\boldsymbol{F} + \boldsymbol{\epsilon}) \\ &\approx \boldsymbol{Z} - \sum_\alpha \Delta\gamma^\alpha \boldsymbol{S}^\alpha \cdot \boldsymbol{\epsilon}\end{aligned} \tag{A.4}$$

where $\boldsymbol{Z} \sim \mathcal{N}(0, 4\boldsymbol{\sigma})$. Let $\tilde{\boldsymbol{f}}(\Delta\boldsymbol{\gamma})$ be the vectorised form of $\boldsymbol{f}(\Delta\boldsymbol{\gamma})$:

$$\tilde{\boldsymbol{f}}(\Delta\boldsymbol{\gamma}) = \begin{bmatrix} f_{11}(\Delta\boldsymbol{\gamma}) & f_{21}(\Delta\boldsymbol{\gamma}) & f_{22}(\Delta\boldsymbol{\gamma}) & f_{12}(\Delta\boldsymbol{\gamma}) \end{bmatrix}^\top$$

Its expectation is:

$$\begin{aligned}\bar{\boldsymbol{f}}(\Delta\boldsymbol{\gamma}) &= E\left[\tilde{\boldsymbol{f}}(\Delta\boldsymbol{\gamma})\right] \\ &= E\left[\mathrm{Vec}\left(\boldsymbol{f}(\Delta\boldsymbol{\gamma})\right)\right] \\ &= -\sum_\alpha \Delta\gamma^\alpha \tilde{\boldsymbol{S}}^\alpha \tilde{\boldsymbol{\mu}}\end{aligned} \tag{A.5}$$

with $\tilde{\boldsymbol{\mu}} = \mathrm{Vec}(\boldsymbol{\mu})$ and $\tilde{\boldsymbol{S}}^\alpha$ being the 4×4 block matrix so that:

$$\mathrm{Vec}\left(\boldsymbol{S}^\alpha \cdot \boldsymbol{\mu}\right) = \tilde{\boldsymbol{S}}^\alpha \tilde{\boldsymbol{\mu}}$$

Let $\boldsymbol{\Sigma}$ be the covariance on $\boldsymbol{f}$. Linear covariances algebra (Feller, 1957, Chap. 3) allows to infer $\boldsymbol{\Sigma}$ from (A.4):

$$\boldsymbol{\Sigma} = \mathrm{Cov}\left[\boldsymbol{Z}\right] + \mathrm{Cov}\left[\boldsymbol{Z}, \sum_\alpha \Delta\gamma^\alpha \boldsymbol{S}^\alpha \cdot \boldsymbol{\epsilon}\right] + \mathrm{Cov}\left[\sum_\alpha \Delta\gamma^\alpha \boldsymbol{S}^\alpha \cdot \boldsymbol{\epsilon}, \boldsymbol{Z}\right]$$

[9] https://fr.mathworks.com/matlabcentral/fileexchange/17555-light-bartlein-color-maps (Retrieved September 3, 2024).

$$+\ \mathrm{Cov}\left[\sum_\alpha \Delta\gamma^\alpha \boldsymbol{S}^\alpha \cdot \boldsymbol{\epsilon}\right]$$

where $\mathrm{Cov}[\boldsymbol{a},\boldsymbol{b}]$ denotes the cross-covariance tensor between tensors $\boldsymbol{a}$ and $\boldsymbol{b}$. Let $\tilde{\boldsymbol{\Sigma}}$ be the 4×4 matrix corresponding to the vectorised form of $\boldsymbol{\Sigma}$. It comes:

$$\tilde{\boldsymbol{\Sigma}} = \mathrm{Cov}\left[\mathrm{Vec}\left(\boldsymbol{Z}\right)\right] + \boldsymbol{A} + \boldsymbol{A}^\top + \boldsymbol{B} \tag{A.6}$$

with:

$$\mathrm{Cov}\left[\mathrm{Vec}\left(\boldsymbol{Z}\right)\right] = \mathrm{Vec}\left(\mathrm{Cov}\left[\boldsymbol{Z}\right]\right) = 4\tilde{\boldsymbol{\sigma}}$$

$$\begin{aligned}\boldsymbol{A} &= \mathrm{Cov}\left[\mathrm{Vec}\left(\boldsymbol{Z}\right), \sum_\alpha \Delta\gamma^\alpha \mathrm{Vec}\left(\boldsymbol{S}^\alpha\cdot\boldsymbol{\epsilon}\right)\right]\\ &= \sum_\alpha \Delta\gamma^\alpha \mathrm{Cov}\left[\mathrm{Vec}\left(\boldsymbol{Z}\right), \mathrm{Vec}\left(\boldsymbol{S}^\alpha\cdot\boldsymbol{\epsilon}\right)\right]\\ &= \sum_\alpha \Delta\gamma^\alpha \mathrm{Cov}\left[\mathrm{Vec}\left(\boldsymbol{Z}\right), \mathrm{Vec}\left(\boldsymbol{\epsilon}\right)\right]\left(\tilde{\boldsymbol{S}}^\alpha\right)^\top\\ &= 2\tilde{\boldsymbol{\sigma}}\sum_\alpha \Delta\gamma^\alpha\left(\tilde{\boldsymbol{S}}^\alpha\right)^\top\end{aligned}$$

and

$$\begin{aligned}\boldsymbol{B} &= \mathrm{Cov}\left[\sum_\alpha \Delta\gamma^\alpha \mathrm{Vec}\left(\boldsymbol{S}^\alpha\cdot\boldsymbol{\epsilon}\right)\right]\\ &= \sum_\alpha\sum_\beta \mathrm{Cov}\left[\Delta\gamma^\alpha \mathrm{Vec}\left(\boldsymbol{S}^\alpha\cdot\boldsymbol{\epsilon}\right), \Delta\gamma^\beta \mathrm{Vec}\left(\boldsymbol{S}^\alpha\cdot\boldsymbol{\epsilon}\right)\right]\\ &= \sum_\alpha\sum_\beta \Delta\gamma^\alpha\Delta\gamma^\beta \tilde{\boldsymbol{S}}^\alpha\tilde{\boldsymbol{\sigma}}\left(\tilde{\boldsymbol{S}}^\beta\right)^\top\end{aligned}$$

To summarise, we have $\tilde{\boldsymbol{f}}\left(\Delta\boldsymbol{\gamma}\right) \sim \mathcal{N}\left(\bar{\boldsymbol{f}}\left(\Delta\boldsymbol{\gamma}\right), \tilde{\boldsymbol{\Sigma}}\left(\Delta\boldsymbol{\gamma}\right)\right)$. The (squared) Mahalanobis distance is defined as Mahalanobis (2018):

$$d^2\left(\boldsymbol{g}\right) = \left(\tilde{\boldsymbol{f}} - \bar{\boldsymbol{f}}\right)^\top \tilde{\boldsymbol{\Sigma}}^{-1}\left(\tilde{\boldsymbol{f}} - \bar{\boldsymbol{f}}\right)$$

According to (A.4) and (A.5), $d^2\left(\Delta\boldsymbol{\gamma}\right) = 0$ if $\boldsymbol{Z} = 0$ (no noise on $\Delta\boldsymbol{F}$) and $\boldsymbol{\epsilon} = \boldsymbol{\mu}$ (the noise on $\mathring{\boldsymbol{F}}$ equals its mean value). In general, we want d^2 to be less than a critical value $d^2_{\max}$, which depends on a significance level. Finally, the Energy method (18) can be changed to:

$$\Delta\boldsymbol{\gamma} = \underset{\boldsymbol{g}}{\mathrm{Arg\,min}}\left\{|\boldsymbol{g}|^\top\left(\frac{\boldsymbol{H}}{2}|\boldsymbol{g}| + \boldsymbol{s}\right) \text{ such that: } d^2\left(\boldsymbol{g}\right) < d^2_{\max}\right\} \tag{A.7}$$

It is worth mentioning that $\boldsymbol{A}$, and a fortiori $\boldsymbol{B}$, can be neglected if $\Delta\gamma^\alpha$ are small enough.

The main difficulty here is to measure $\boldsymbol{\mu}(x,y)$ and $\boldsymbol{\sigma}(x,y)$, as introduced in (A.2). This can be done by acquiring multiple SEM images of the same area, with no strain, then applying DIC on them. However, this task can be very time-consuming in case of stitched images, as in the current work.

Appendix B. Gradient and Hessian of the cost and constraint functions

B.1. The L_1-norm

By definition, the L_1-norm is:

$$\|\boldsymbol{g}\|_1 = \sum_\alpha |g_\alpha|$$

Hence, the gradient of the L_1 norm is simply:

$$\nabla_i\left(\|\boldsymbol{g}\|_1\right) = \mathrm{sign}\left(g_i\right)$$

Therefore, the Hessian of the L_1-norm is null.

B.2. The Energy function

The gradient of the Energy function, as defined in (17), is:

$$\begin{aligned}\nabla_i\left(w\right) &= \frac{\partial w\left(\boldsymbol{g}\right)}{\partial g_i}\\ &= \frac{\partial w}{\partial|g_i|}\frac{\partial|g_i|}{\partial g_i}\\ &= \left(H_{ik}|g_k| + s_i\right)\mathrm{sign}\left(g_i\right)\end{aligned}$$

whereas its Hessian is:

$$\begin{aligned}\nabla^2_{ij}\left(w\right) &= \frac{\partial^2 w\left(\boldsymbol{g}\right)}{\partial g_i\partial g_j}\\ &= \frac{\partial\left(H_{ik}|g_k| + s_i\right)}{\partial g_j}\mathrm{sign}\left(g_i\right)\\ &= \left(H_{ik}\frac{\partial|g_k|}{\partial g_j}\right)\mathrm{sign}\left(g_i\right)\\ &= H_{ik}\delta_{jk}\mathrm{sign}\left(g_k\right)\mathrm{sign}\left(g_i\right)\\ &= H_{ij}\mathrm{sign}\left(g_i g_j\right)\ .\end{aligned}$$

B.3. The Mahalanobis distance

The gradient of the Mahalanobis distance is:

$$\begin{aligned}\nabla_i\left(d^2\right) &= \frac{\partial\left(d^2\left(\boldsymbol{g}\right)\right)}{\partial g_i}\\ &= \frac{\partial}{\partial g_i}\left[\left(\tilde{f}_k - \bar{f}_k\right)\tilde{\Sigma}^{-1}_{k\ell}\left(\tilde{f}_\ell - \bar{f}_\ell\right)\right]\\ &= 2\Sigma^{-1}_{k\ell}\left(\tilde{f}_k - \bar{f}_k\right)\frac{\partial}{\partial g_i}\left(\tilde{f}_\ell - \bar{f}_\ell\right) + \left(\tilde{f}_k - \bar{f}_k\right)\frac{\partial\tilde{\Sigma}^{-1}_{k\ell}}{\partial g_i}\left(\tilde{f}_\ell - \bar{f}_\ell\right)\end{aligned} \tag{B.1}$$

Eq. (A.3) gives:

$$\begin{aligned}\frac{\partial\tilde{\boldsymbol{f}}\left(\boldsymbol{g}\right)}{\partial g_i} &= -\frac{\partial}{\partial g_i}\left(\sum_\alpha g_\alpha \mathrm{Vec}\left(\boldsymbol{S}^\alpha\cdot\boldsymbol{F}^\theta\right)\right)\\ &= -\frac{\partial}{\partial g_i}\left(\sum_\alpha g_\alpha\tilde{\boldsymbol{S}}^\alpha\tilde{\boldsymbol{F}}\right)\\ &= -\tilde{\boldsymbol{S}}^i\tilde{\boldsymbol{F}}\end{aligned}$$

Similarly, (A.5) reads:

$$\frac{\partial\bar{\boldsymbol{f}}\left(\boldsymbol{g}\right)}{\partial g_i} = -\tilde{\boldsymbol{S}}^i\tilde{\boldsymbol{\mu}}$$

Therefore:

$$\begin{aligned}\frac{\partial\tilde{f}_\ell}{\partial g_i} - \frac{\partial\bar{f}_\ell}{\partial g_i} &= -\left[\tilde{\boldsymbol{S}}^i\left(\tilde{\boldsymbol{F}} - \tilde{\boldsymbol{\mu}}\right)\right]_\ell\\ &= \tilde{S}^i_{\ell q}\left(\tilde{E}_q - \tilde{F}_q\right)\end{aligned} \tag{B.2}$$

Analytical equation for $\frac{\partial\tilde{\Sigma}^{-1}_{k\ell}}{\partial g_j}$ in (B.1) is hard to estimate, but one can neglect $\boldsymbol{B}$ in (A.6), so that:

$$\tilde{\boldsymbol{\Sigma}} \approx 4\tilde{\boldsymbol{\sigma}}\left(\boldsymbol{\delta} + \frac{1}{2}\left(\boldsymbol{D}^\top + \tilde{\boldsymbol{\sigma}}^{-1}\boldsymbol{D}\tilde{\boldsymbol{\sigma}}\right)\right) \tag{B.3}$$

with

$$\boldsymbol{D}\left(\boldsymbol{g}\right) = \sum_i g_i\tilde{\boldsymbol{S}}^i \tag{B.4}$$

and $\boldsymbol{\delta}$ the $N\times N$ identity matrix. One can easily demonstrate that the infinity norms of $\boldsymbol{D}$ and $\tilde{\boldsymbol{\sigma}}^{-1}\boldsymbol{D}\tilde{\boldsymbol{\sigma}}$ are below unity; thus, the truncated Neumann series of the inverse of (B.3) gives:

$$\begin{aligned}\boldsymbol{\Sigma}^{-1} &\approx \left(\boldsymbol{\delta} - \frac{1}{2}\left(\boldsymbol{D}^\top + \tilde{\boldsymbol{\sigma}}^{-1}\boldsymbol{D}\tilde{\boldsymbol{\sigma}}\right)\right)\frac{\tilde{\boldsymbol{\sigma}}^{-1}}{4}\\ &\approx \frac{\tilde{\boldsymbol{\sigma}}^{-1}}{4} - \frac{1}{8}\left(\boldsymbol{D}^\top\tilde{\boldsymbol{\sigma}}^{-1} + \tilde{\boldsymbol{\sigma}}^{-1}\boldsymbol{D}\right)\ .\end{aligned} \tag{B.5}$$

Therefore, (B.4) and (B.5) read:

$$\frac{\partial \tilde{\Sigma}^{-1}_{k\ell}}{\partial g_i} \approx \frac{-1}{8}\left(\frac{\partial D_{qk}}{\partial g_i}\tilde{\sigma}^{-1}_{q\ell} + \tilde{\sigma}^{-1}_{kq}\frac{\partial D_{q\ell}}{\partial g_i}\right) \approx \frac{-1}{8}\left(\tilde{\sigma}^{-1}_{q\ell}\tilde{S}^i_{qk} + \tilde{\sigma}^{-1}_{kq}\tilde{S}^i_{q\ell}\right) \tag{B.6}$$

Combining (B.1), (B.2) and (B.6) gives:

$$\nabla_i\left(d^2\right) = \left(\tilde{f}_k - \bar{f}_k\right)\left[2\tilde{\Sigma}^{-1}_{k\ell}\tilde{S}^i_{\ell q}\left(\tilde{E}_q - \bar{F}_q\right) - \frac{1}{8}\left(\tilde{\sigma}^{-1}_{q\ell}S^i_{qk} + \tilde{\sigma}^{-1}_{kq}S^i_{q\ell}\right)\left(\tilde{f}_\ell - \bar{f}_\ell\right)\right] \tag{B.7}$$

$$= \left(\tilde{\boldsymbol{f}} - \bar{\boldsymbol{f}}\right)^\top\left[2\tilde{\boldsymbol{\Sigma}}^{-1}\boldsymbol{S}^i\left(\tilde{\boldsymbol{\mu}} - \bar{\boldsymbol{F}}\right) - \frac{1}{8}\left(\tilde{\boldsymbol{\sigma}}^{-1}\boldsymbol{S}^i + \left(\tilde{\boldsymbol{\sigma}}^{-1}\boldsymbol{S}^i\right)^\top\right)\left(\tilde{\boldsymbol{f}} - \bar{\boldsymbol{f}}\right)\right]$$

According to (B.7), the Hessian of the Mahalanobis distance is:

$$\nabla^2_{ij}\left(d^2\right) = \frac{\partial\left(\tilde{f}_k - \bar{f}_k\right)}{\partial g_j}\left[2\tilde{\Sigma}^{-1}_{k\ell}\tilde{S}^i_{\ell q}\left(\tilde{E}_q - \bar{F}_q\right) - \frac{1}{8}\left(\tilde{\sigma}^{-1}_{q\ell}\tilde{S}^i_{qk} + \tilde{\sigma}^{-1}_{kq}\tilde{S}^i_{q\ell}\right)\left(\tilde{f}_\ell - \bar{f}_\ell\right)\right] + \left(\tilde{f}_k - \bar{f}_k\right)\left[2\frac{\partial\tilde{\Sigma}^{-1}_{k\ell}}{\partial g_j}\tilde{S}^i_{\ell q}\left(\tilde{E}_q - \bar{F}_q\right) - \frac{1}{8}\left(\tilde{\sigma}^{-1}_{q\ell}\tilde{S}^i_{qk} + \tilde{\sigma}^{-1}_{kq}\tilde{S}^i_{q\ell}\right)\frac{\partial\left(\tilde{f}_\ell - \bar{f}_\ell\right)}{\partial g_j}\right]$$

Eqs. (B.2) and (B.6) give:

$$\nabla^2_{ij}\left(d^2\right) = \tilde{S}^j_{kp}\left(\tilde{E}_p - \bar{F}_p\right)\left[2\tilde{\Sigma}^{-1}_{k\ell}\tilde{S}^i_{\ell q}\left(\tilde{E}_q - \bar{F}_q\right) - \frac{1}{8}\left(\tilde{\sigma}^{-1}_{q\ell}\tilde{S}^i_{qk} + \tilde{\sigma}^{-1}_{kq}\tilde{S}^i_{q\ell}\right)\left(\tilde{f}_\ell - \bar{f}_\ell\right)\right] + \left(\tilde{f}_k - \bar{f}_k\right)\left[\frac{-1}{4}\left(\tilde{\sigma}^{-1}_{q\ell}\tilde{S}^j_{qk} + \tilde{\sigma}^{-1}_{kq}\tilde{S}^j_{q\ell}\right)\tilde{S}^i_{\ell q} - \frac{1}{8}\left(\tilde{\sigma}^{-1}_{q\ell}\tilde{S}^i_{qk} + \tilde{\sigma}^{-1}_{kq}\tilde{S}^i_{q\ell}\right)\tilde{S}^j_{\ell q}\right]\left(\tilde{E}_q - \bar{F}_q\right) \tag{B.8}$$

Taking advantage of the symmetry of $\tilde{\sigma}^{-1}_{q\ell}\tilde{S}^i_{qk} + \tilde{\sigma}^{-1}_{kq}\tilde{S}^i_{q\ell}$ in (B.8), one can recognise that:

$$\tilde{S}^j_{kp}\left(\tilde{E}_p - \bar{F}_p\right)\left(\tilde{\sigma}^{-1}_{q\ell}\tilde{S}^i_{qk} + \tilde{\sigma}^{-1}_{kq}\tilde{S}^i_{q\ell}\right)\left(\tilde{f}_\ell - \bar{f}_\ell\right) = \left(\tilde{f}_k - \bar{f}_k\right) \times \left(\tilde{\sigma}^{-1}_{q\ell}\tilde{S}^i_{qk} + \tilde{\sigma}^{-1}_{kq}\tilde{S}^i_{q\ell}\right)\tilde{S}^j_{\ell q}\left(\tilde{E}_q - \bar{F}_q\right)$$

Therefore, the Hessian of the Mahalanobis distance is:

$$\nabla^2_{ij}\left(d^2\right) = \left(\tilde{E}_p - \bar{F}_p\right)\left[2\tilde{S}^j_{kp}\tilde{\Sigma}^{-1}_{k\ell}\tilde{S}^i_{\ell q}\left(\tilde{E}_q - \bar{F}_q\right) - \frac{1}{4}T^{ij}_{p\ell}\left(\tilde{f}_\ell - \bar{f}_\ell\right)\right] \tag{B.9}$$

with

$$T^{ij}_{p\ell} = \tilde{S}^j_{kp}\left(\tilde{\sigma}^{-1}_{q\ell}\tilde{S}^i_{qk} + \tilde{\sigma}^{-1}_{kq}\tilde{S}^i_{q\ell}\right) + \tilde{S}^i_{kp}\left(\tilde{\sigma}^{-1}_{q\ell}\tilde{S}^j_{qk} + \tilde{\sigma}^{-1}_{kq}\tilde{S}^j_{q\ell}\right) \tag{B.10}$$

Eqs. (B.9) and (B.10) are equivalent to:

$$\nabla^2_{ij}\left(d^2\right) = \left(\tilde{\boldsymbol{\mu}} - \bar{\boldsymbol{F}}\right)^\top\left[2\left(\tilde{\boldsymbol{S}}^j\right)^\top\tilde{\boldsymbol{\Sigma}}^{-1}\tilde{\boldsymbol{S}}^i\left(\boldsymbol{E} - \boldsymbol{F}\right) - \frac{1}{4}\boldsymbol{T}^{ij}\left(\tilde{\boldsymbol{f}} - \bar{\boldsymbol{f}}\right)\right]$$

with

$$\boldsymbol{T}^{ij} = \left(\tilde{\boldsymbol{S}}^j\right)^\top\left(\tilde{\boldsymbol{\sigma}}^{-1}\tilde{\boldsymbol{S}}^i + \left(\tilde{\boldsymbol{\sigma}}^{-1}\tilde{\boldsymbol{S}}^i\right)^\top\right) + \left(\tilde{\boldsymbol{S}}^i\right)^\top\left(\tilde{\boldsymbol{\sigma}}^{-1}\tilde{\boldsymbol{S}}^j + \left(\tilde{\boldsymbol{\sigma}}^{-1}\tilde{\boldsymbol{S}}^j\right)^\top\right)$$

References

Bachmann, F., Hielscher, R., Schaeben, H., 2010. Texture analysis with MTEX–free and open source software toolbox. Solid State Phenom. 160, 63–68.

Bachmann, F., Hielscher, R., Schaeben, H., 2011. Grain detection from 2d and 3d EBSD data—Specification of the MTEX algorithm. Ultramicroscopy 111 (12), 1720–1733.

Blaber, J., Adair, B., Antoniou, A., 2015. Ncorr: open-source 2D digital image correlation matlab software. Exp. Mech. 55 (6), 1105–1122.

Bourdin, F., Stinville, J., Echlin, M., Callahan, P., Lenthe, W., Torbet, C., Texier, D., Bridier, F., Cormier, J., Villechaise, P., Pollock, T., Valle, V., 2018. Measurements of plastic localization by heaviside-digital image correlation. Acta Mater. (ISSN: 1359-6454) 157, 307–325. http://dx.doi.org/10.1016/j.actamat.2018.07.013, URL https://www.sciencedirect.com/science/article/pii/S135964541830541X.

Brosius, A., Küsters, N., Lenzen, M., 2018. New method for stress determination based on digital image correlation data. CIRP Ann (ISSN: 0007-8506) 67 (1), 269–272. http://dx.doi.org/10.1016/j.cirp.2018.04.026, URL https://www.sciencedirect.com/science/article/pii/S0007850618300507.

Charpagne, M., Stinville, J., Callahan, P., Texier, D., Chen, Z., Villechaise, P., Valle, V., Pollock, T., 2020. Automated and quantitative analysis of plastic strain localization via multi-modal data recombination. Mater. Charact. (ISSN: 1044-5803) 163, 110245. http://dx.doi.org/10.1016/j.matchar.2020.110245, URL https://www.sciencedirect.com/science/article/pii/S1044580319335569.

Chen, Z., Daly, S., 2017. Active slip system identification in polycrystalline metals by digital image correlation (DIC). Exp. Mech. 57, 115–127. http://dx.doi.org/10.1007/s11340-016-0217-3.

Depriester, D., Goulmy, J., Barrallier, L., 2023. Crystal plasticity simulations of in situ tensile tests: A two-step inverse method for identification of CP parameters, and assessment of CPFEM capabilities. Int. J. Plast. (ISSN: 0749-6419) 168, 103695. http://dx.doi.org/10.1016/j.ijplas.2023.103695, URL https://www.sciencedirect.com/science/article/pii/S074964192300181X.

Depriester, D., Kubler, R., 2020. MTEX2Gmsh: a tool for generating 2D meshes from EBSD data. J. Open Source Softw. 5 (52), 2094. http://dx.doi.org/10.21105/joss.02094.

Di Gioacchino, F., Edwards, T.E.J., Wells, G.N., Clegg, W.J., 2020. A new mechanism of strain transfer in polycrystals. Sci. Rep. (ISSN: 2045-2322) 10 (1), 10082. http://dx.doi.org/10.1038/s41598-020-66569-7, URL http://www.nature.com/articles/s41598-020-66569-7.

Di Gioacchino, F., Quinta da Fonseca, J., 2015. An experimental study of the polycrystalline plasticity of austenitic stainless steel. Int. J. Plast. (ISSN: 0749-6419) 74, 92–109. http://dx.doi.org/10.1016/j.ijplas.2015.05.012, URL http://www.sciencedirect.com/science/article/pii/S0749641915000820.

Feller, W., 1957. An introduction to probability theory and its applications, second ed. In: A Wiley Publication in Mathematical Statistics, Wiley, New York, ISBN: 978-0-471-25709-7.

Githens, A., Ganesan, S., Chen, Z., Allison, J., Sundararaghavan, V., Daly, S., 2020. Characterizing microscale deformation mechanisms and macroscopic tensile properties of a high strength magnesium rare-earth alloy: A combined experimental and crystal plasticity approach. Acta Mater. (ISSN: 1359-6454) 186, 77–94. http://dx.doi.org/10.1016/j.actamat.2019.12.012.

Goodfellow, I., Bengio, Y., Courville, A., 2016. Deep Learning. MIT Press, http://www.deeplearningbook.org.

Goulmy, J., Depriester, D., Guittonneau, F., Barrallier, L., Jégou, S., 2022. Mechanical behavior of polycrystals: Coupled in situ DIC-EBSD analysis of pure copper under tensile test. Mater. Charact. 194, 112322, Publisher: Elsevier.

Goulmy, J.P., Guittonneau, F., Jégou, S., Barrallier, L., 2024. Classification of the acquisition conditions driving the accuracy of strain measurements during in situ DIC with scanning electron microscope. Strain 60 (1), e12456. http://dx.doi.org/10.1111/str.12456, arXiv:https://onlinelibrary.wiley.com/doi/pdf/10.1111/str.12456, URL https://onlinelibrary.wiley.com/doi/abs/10.1111/str.12456.

Guan, Y., Chen, B., Zou, J., Britton, T.B., Jiang, J., Dunne, F.P.E., 2017. Crystal plasticity modelling and HR-DIC measurement of slip activation and strain localization in single and oligo-crystal Ni alloys under fatigue. Int. J. Plast. (ISSN: 0749-6419) 88, 70–88. http://dx.doi.org/10.1016/j.ijplas.2016.10.001, URL https://www.sciencedirect.com/science/article/pii/S0749641916301978.

Guan, X.X., Lu, L., Luo, S.N., Fan, D., 2021. In situ observations of detwinning and strain localization in pure titanium. Mater. Sci. Eng. A (ISSN: 0921-5093) 813, 141073. http://dx.doi.org/10.1016/j.msea.2021.141073, URL https://www.sciencedirect.com/science/article/pii/S0921509321003427.

Guery, A., Hild, F., Latourte, F., Roux, S., 2016a. Identification of crystal plasticity parameters using DIC measurements and weighted FEMU. Mech. Mater. (ISSN: 0167-6636) 100, 55–71. http://dx.doi.org/10.1016/j.mechmat.2016.06.007.

Guery, A., Hild, F., Latourte, F., Roux, S., 2016b. Slip activities in polycrystals determined by coupling DIC measurements with crystal plasticity calculations. Int. J. Plast. (ISSN: 0749-6419) 81, 249–266. http://dx.doi.org/10.1016/j.ijplas.2016.01.008, URL https://www.sciencedirect.com/science/article/pii/S0749641916000188.

Hall, B.C., 2013. Lie groups, Lie algebras, and representations. In: Quantum Theory for Mathematicians. Springer, pp. 333–366.

Harte, A., Atkinson, M., Smith, A., Drouven, C., Zaefferer, S., Quinta da Fonseca, J., Preuss, M., 2020. The effect of solid solution and gamma prime on the deformation modes in Ni-based superalloys. Acta Mater. (ISSN: 1359-6454) 194, 257–275. http://dx.doi.org/10.1016/j.actamat.2020.04.004, URL https://www.sciencedirect.com/science/article/pii/S1359645420302615.

Héripré, E., Dexet, M., Crépin, J., Gélébart, L., Roos, A., Bornert, M., Caldemaison, D., 2007. Coupling between experimental measurements and polycrystal finite element calculations for micromechanical study of metallic materials. Int. J. Plast. (ISSN: 0749-6419) 23 (9), 1512–1539. http://dx.doi.org/10.1016/j.ijplas.2007.01.009.

Iftikhar, C.M.A., Brahme, A., Inal, K., Khan, A.S., 2022. An evolution of subsequent yield loci under proportional and non-proportional loading path of 'as-received' extruded AZ31 magnesium alloy: Experiments and CPFEM modeling. Int. J. Plast. (ISSN: 0749-6419) 151, 103216. http://dx.doi.org/10.1016/j.ijplas.2022.103216, URL https://www.sciencedirect.com/science/article/pii/S0749641922000043.

Jackson, A.G., 2012. Handbook of Crystallography: for Electron Microscopists and Others. Springer Science & Business Media.

Kalidindi, S., Bronkhorst, C., Anand, L., 1992. Crystallographic texture evolution in bulk deformation processing of FCC metals. J. Mech. Phys. Solids (ISSN: 0022-5096) 40 (3), 537–569. http://dx.doi.org/10.1016/0022-5096(92)80003-9.

Kawano, Y., Ohashi, T., Mayama, T., Tanaka, M., Okuyama, Y., Sato, M., 2019. Investigation of strain redistribution mechanism in α titanium by image-based crystal plasticity analysis. Eur. Phys. J. B 92 (9), 1–10. http://dx.doi.org/10.1140/epjb/e2019-100238-3.

Kocks, U., 1970. The relation between polycrystal deformation and single-crystal deformation. Metall. Mater. Trans. B 1, 1121–1143.

León-Cázares, F.D., Rowlands, B., Galindo-Nava, E.I., 2023. Quantification of slip band distribution in polycrystals: An automated fast Fourier transform decomposition approach. Microsc. Microanal. (ISSN: 1431-9276) 29 (2), 580–595. http://dx.doi.org/10.1093/micmic/ozad002, arXiv:https://academic.oup.com/mam/article-pdf/29/2/580/49764551/ozad002.pdf.

Light, A., Bartlein, P.J., 2004. The end of the rainbow? Color schemes for improved data graphics. EOS Trans. Am. Geophys. Union 85 (40), 385–391. http://dx.doi.org/10.1029/2004EO400002 (ISSN 0096-3941) URL https://agupubs.onlinelibrary.wiley.com/doi/10.1029/2004EO400002.

Mahalanobis, P.C., 2018. On the generalized distance in statistics. Sankhyā: Ind. J. Stat. Ser. A (2008-) 80, S1–S7.

Maraghechi, S., Hoefnagels, J., Peerlings, R., Rokoš, O., Geers, M., 2019. Correction of scanning electron microscope imaging artifacts in a novel digital image correlation framework. Exp. Mech. 59, 489–516. http://dx.doi.org/10.1007/s11340-018-00469-w.

Mello, A.W., Book, T.A., Nicolas, A., Otto, S.E., Gilpin, C.J., Sangid, M.D., 2017. Distortion correction protocol for digital image correlation after scanning electron microscopy: Emphasis on long duration and ex-situ experiments. Exp. Mech. (ISSN: 1741-2765) 57 (9), 1395–1409. http://dx.doi.org/10.1007/s11340-017-0303-1.

Nemat-Nasser, S., 2004. Plasticity: a Treatise on Finite Deformation of Heterogeneous Inelastic Materials. Cambridge University Press.

Peirce, D., Asaro, R., Needleman, A., 1982. An analysis of nonuniform and localized deformation in ductile single crystals. Acta Metall. (ISSN: 0001-6160) 30 (6), 1087–1119. http://dx.doi.org/10.1016/0001-6160(82)90005-0.

Press, W.H., 2007. Numerical Recipes: the Art of Scientific Computing, third ed. Cambridge University Press, Cambridge, UK, ISBN: 978-0-511-33555-6, OCLC: 748025266.

Rouwane, A., Texier, D., Périé, J.N., Dufour, J.E., Stinville, J.C., Passieux, J.C., 2024. High resolution and large field of view imaging using a stitching procedure coupled with distortion corrections. Opt. Laser Technol. (ISSN: 0030-3992) 177, 111165. http://dx.doi.org/10.1016/j.optlastec.2024.111165, URL https://www.sciencedirect.com/science/article/pii/S0030399224006236.

Roux, S., Réthoré, J., Hild, F., 2009. Digital image correlation and fracture: an advanced technique for estimating stress intensity factors of 2D and 3D cracks. J. Phys. D: Appl. Phys. 42 (21), 214004. http://dx.doi.org/10.1088/0022-3727/42/21/214004.

Salvini, M., Grilli, N., Demir, E., He, S., Martin, T., Flewitt, P., Mostafavi, M., Truman, C., Knowles, D., 2024. Effect of grain boundary misorientation and carbide precipitation on damage initiation: A coupled crystal plasticity and phase field damage study. Int. J. Plast. (ISSN: 0749-6419) 172, 103854. http://dx.doi.org/10.1016/j.ijplas.2023.103854, URL https://www.sciencedirect.com/science/article/pii/S0749641923003388.

Sperry, R., Harte, A., Quinta da Fonseca, J., Homer, E.R., Wagoner, R.H., Fullwood, D.T., 2020. Slip band characteristics in the presence of grain boundaries in nickel-based superalloy. Acta Mater. (ISSN: 1359-6454) 193, 229–238. http://dx.doi.org/10.1016/j.actamat.2020.04.037, URL https://www.sciencedirect.com/science/article/pii/S1359645420303025.

Stinville, J., Charpagne, M., Maaß, R., Proudhon, H., Ludwig, W., Callahan, P., Wang, F., Beyerlein, I., Echlin, M., Pollock, T., 2023. Insights into plastic localization by crystallographic slip from emerging experimental and numerical approaches. Annu. Rev. Mater. Res. (ISSN: 1545-4118) 53 (Volume 53, 2023), 275–317. http://dx.doi.org/10.1146/annurev-matsci-080921-102621, URL https://www.annualreviews.org/content/journals/10.1146/annurev-matsci-080921-102621.

Thiruselvam, N.I., Jeyaraam, R., Subramanian, S.J., Sankaran, S., 2021. Deformation heterogeneity in copper oligocrystals using high-resolution stereo DIC. Materialia (ISSN: 2589-1529) 18, 101164. http://dx.doi.org/10.1016/j.mtla.2021.101164, URL https://www.sciencedirect.com/science/article/pii/S2589152921001678.

Thomas, R., Lunt, D., Atkinson, M.D., Quinta da Fonseca, J., Preuss, M., Barton, F., O'Hanlon, J., Frankel, P., 2019. Characterisation of irradiation enhanced strain localisation in a zirconium alloy. Materialia (ISSN: 2589-1529) 5, 100248. http://dx.doi.org/10.1016/j.mtla.2019.100248, URL https://www.sciencedirect.com/science/article/pii/S2589152919300444.

Vermeij, T., Peerlings, R.H.J., Geers, M.G.D., Hoefnagels, J.P.M., 2023. Automated identification of slip system activity fields from digital image correlation data. Acta Mater. (ISSN: 1359-6454) 243, 118502. http://dx.doi.org/10.1016/j.actamat.2022.118502, URL https://www.sciencedirect.com/science/article/pii/S1359645422008795.

Vermeij, T., Slokker, G., Mornout, C., König, D., Hoefnagels, J., 2024. + SSLIP: Automated radon-assisted and rotation-corrected identification of complex HCP slip system activity fields from DIC data. arXiv preprint arXiv:2408.01087.

Wang, L., Zheng, Z., Phukan, H., Kenesei, P., Park, J.-S., Lind, J., Suter, R., Bieler, T., 2017. Direct measurement of critical resolved shear stress of prismatic and basal slip in polycrystalline Ti using high energy X-ray diffraction microscopy. Acta Mater. (ISSN: 1359-6454) 132, 598–610. http://dx.doi.org/10.1016/j.actamat.2017.05.015, URL https://www.sciencedirect.com/science/article/pii/S1359645417303920.

Yaghoobi, M., Ganesan, S., Sundar, S., Lakshmanan, A., Rudraraju, S., Allison, J.E., Sundararaghavan, V., 2019. PRISMS-plasticity: An open-source crystal plasticity finite element software. Comput. Mater. Sci. (ISSN: 0927-0256) 169, 109078. http://dx.doi.org/10.1016/j.commatsci.2019.109078, URL https://www.sciencedirect.com/science/article/pii/S0927025619303696.

Zecevic, M., Beyerlein, I.J., Knezevic, M., 2018. Activity of pyramidal I and II <c+a> slip in Mg alloys as revealed by texture development. J. Mech. Phys. Solids (ISSN: 0022-5096) 111, 290–307. http://dx.doi.org/10.1016/j.jmps.2017.11.004, URL https://www.sciencedirect.com/science/article/pii/S0022509617307779.